

# Imbalanced TGF $\beta$ signalling and autophagy drive erythroid priming of hematopoietic stem cells in $\beta$ -thalassemia

---

Received: 2 June 2024

---

Accepted: 28 May 2025

---

Published online: 01 July 2025

---

 Check for updates

---

Maria Rosa Lidonnici<sup>1</sup>✉, Giulia Chianella<sup>1,2</sup>, Nicole Mende<sup>3</sup>, Hugo P. Bastos<sup>3</sup>, Matteo Barcella<sup>1</sup>, Ivan Merelli<sup>4</sup>, Mariangela Storto<sup>1</sup>, Valentina Romeo<sup>1</sup>, Francesca Tiboni<sup>1</sup>, Samantha Scaramuzza<sup>1</sup>, Claudia Rossi<sup>1</sup>, Laura Raggi<sup>1</sup>, Annamaria Aprile<sup>1</sup>, Stefania Crippa<sup>1</sup>, Deena Iskander<sup>5</sup>, Irene Roberts<sup>6</sup>, Anastasios Karamiditris<sup>5</sup>, Julia Keith<sup>7</sup>, Christophe Lechauve<sup>7</sup>, Mitchell J. Weiss<sup>7</sup>, Nicola K. Wilson<sup>3</sup>, Berthold Göttgens<sup>3</sup>, Maria Ester Bernardo<sup>1,2,8,9</sup>, Fabio Ciceri<sup>1,2,9</sup>, Alessandro Aiuti<sup>1,2,8,9</sup>, Sarah Markt<sup>1,9</sup>, Elisa Laurenti<sup>3</sup> & Giuliana Ferrari<sup>1,2</sup>✉

---

The hematopoietic stem cell and multipotent progenitor (HSC/MPP) pool dynamically responds to stress to adapt blood output to specific physiological demands. In  $\beta$ -thalassemia (Bthal), severe anemia and ineffective erythropoiesis generate expansion of erythroid precursors and a chronic stress status in the bone marrow (BM) microenvironment. However, the response to the BM altered status at the level of the HSC/MPP compartment in terms of lineage commitment has not been investigated. Bulk and single-cell RNA-sequencing reveal that Bthal HSCs/MPPs are expanded and activated with enhanced priming along the whole Ery differentiation trajectory. Consistently, HSC/MPP showed an altered TGF $\beta$  expression and autophagy transcriptional signatures along with a declined dormancy state. We discovered that the altered TGF $\beta$  signaling fosters the Ery potential of HSCs by reducing their autophagic levels, and *in vivo* stimulation of autophagy is sufficient to rescue the imbalance of the HSC compartment. Our findings identify the interplay between TGF $\beta$  and HSC autophagy as a key driver in the context of non-malignant hematopoiesis.

Hematopoiesis is a continuous and dynamic process through which lifelong blood cells arise daily in the adult bone marrow (BM)<sup>1</sup>. It has been historically described as a binary cell fate tree with a hierarchical development from multipotent hematopoietic stem cells (HSCs) to unipotent progenitors. The main lineage restriction event was represented by the segregation of the multipotent progenitors (MPPs) into

common lymphoid progenitors (CLPs) and common myeloid progenitors (CMPs)<sup>2,3</sup>.

During the last decade, single-cell resolution and transcriptomic studies challenged this view of a hierarchical development, depicting an innovative model of hematopoiesis, in which the hierarchy road-map is flexibly adapting to different conditions by engaging stem and

---

<sup>1</sup>San Raffaele-Telethon Institute for Gene Therapy (SR-TIGET), IRCCS San Raffaele Scientific Institute, Milan, Italy. <sup>2</sup>University Vita-Salute San Raffaele, Milan, Italy. <sup>3</sup>Wellcome-MRC Cambridge Stem Cell Institute, Department of Haematology, Jeffrey Cheah Biomedical Centre, University of Cambridge, Cambridge, UK. <sup>4</sup>Institute for Biomedical Technologies, National Research Council, Segrate, Italy. <sup>5</sup>Department of Immunology & Inflammation, Imperial College London, London, UK. <sup>6</sup>Department of Paediatrics, University of Oxford, Oxford, UK. <sup>7</sup>Department of Hematology, St. Jude Children's Research Hospital, Memphis, TN, USA. <sup>8</sup>Pediatric Immunohematology, IRCCS San Raffaele Scientific Institute, Milan, Italy. <sup>9</sup>Haematology and BMT Unit IRCCS San Raffaele Scientific Institute, Milan, Italy. ✉e-mail: [lidonnici.mariarosa@hsr.it](mailto:lidonnici.mariarosa@hsr.it); [ferrari.giuliana@hsr.it](mailto:ferrari.giuliana@hsr.it)

progenitor cell populations<sup>4,5</sup>. Thus, the HSC pool is molecularly and functionally heterogeneous in terms of cell cycle, differentiation properties and engraftment capacity<sup>6</sup>. Upon transplantation HSCs display a wide-range of potentials with lineage-biases, giving rise to myeloid (My) and lymphoid (Ly) cells, and platelets (PLTs)<sup>7,8</sup>. Several studies recently indicated that the HSC lineage fate decision might occur within the most primitive compartment<sup>1,9–11</sup>. The first segregation between multipotent long-term repopulating cells with erythroid-myeloid-lymphoid (Ery/My/Ly) potential (Subset1) and cells with My/Ly only (Subset2), takes place within the HSC/MPP and CD49f+ HSC population<sup>11</sup>. In addition, it has been hypothesized that HSC/MPP with Ery-only differentiation<sup>11</sup> may coincide with human erythroid-restricted MPP<sup>10,11</sup>. In this scenario, the heterogeneous HSC pool can be considered as an emergency supporter, to replenish cell deficiency of specific lineages<sup>7,12</sup>, rather than a continuous source of differentiating blood cells. Under unperturbed conditions, adult HSCs reside mostly in a quiescent<sup>13</sup>, glycolytic<sup>14</sup>, and autophagy-dependent<sup>15</sup> state. On the contrary, several stress conditions, such as inflammation, anemia, and infections<sup>16</sup>, induce dormant HSCs into the cell cycle affecting their lineage commitment<sup>13,17,18</sup>. More recently, this concept has been argued by the role of MPPs as the major source for blood cell production in response to stress<sup>19,20</sup>. In this continuous evolving landscape, how lineage commitment is normally regulated and disrupted in stress conditions remains unaddressed.

Bthal is a chronic genetic anemia due to mutations in the  $\beta$ -globin gene, leading to abnormal synthesis of adult hemoglobin, chronic expansion of BM erythroblasts with defective Ery cell maturation and red blood cell (RBC) production and survival<sup>21</sup>. Notably, we recently unveiled a general perturbed and stress condition of the BM micro-environment with both cellular and molecular components affected<sup>22,23</sup>. In the peripheral blood, Bthal patients have circulating HSC/MPPs skewed towards an increased My production over the Ery lineage<sup>24</sup>, suggestive of triggering events in the BM at the level of HSC/MPP leading to unbalanced differentiation and/or skewed mobilization. Thus, Bthal represents an ideal natural model to elucidate the regulation of HSC lineage specification and differentiation at the level of HSC/MPP in a model of perturbed but non-malignant hematopoiesis.

We performed transcriptome analysis at single-cell level in Bthal HSCs/MPPs to reveal the cell composition and uncover deregulated pathways to identify the major players affecting lineage fate choice. Findings in patients' samples were functionally proven in vivo in the murine disease model, leading to the discovery of the key driving molecules and pathways. Overall, these analyses provide new insights into mechanisms coordinating HSC lineage differentiation in perturbed stress BM conditions.

## Results

### Defective hematopoietic process in Bthal patients

We first evaluated the content of long-term hematopoietic stem cells (LT-HSCs) and different progenitors (multipotent progenitors, MPPs; common myeloid progenitors, CMPs; megakaryocytic-erythroid progenitors, MEPs; granulocyte-monocyte progenitors, GMPs; multipotent lymphoid progenitors, MLPs) in the BM samples collected from transfusion-dependent thalassemia (TDT) patients and healthy donors (HD), using specific cell surface markers (Fig. S1–S2). We showed no difference in the percentage of phenotypic LT-HSCs, but an increase in MPPs in Bthal samples irrespective of the age (Fig. 1A, B, Fig. S3A, B). By evaluating the CD71 and BAH1 expression that efficiently resolved My, Ery, and Mk lineage fates<sup>10</sup>, we quantified the recently identified Ery subsets (CD71<sup>+</sup>BAH1<sup>+</sup>) within progenitors (CD34<sup>+</sup>CD38<sup>+</sup>) and primitive MPPs (CD34<sup>+</sup>CD38<sup>+</sup>CD45RA<sup>+</sup>CD90<sup>+</sup>) (Fig. S4A) and observed a reduction of Ery progenitors in both compartments (Fig. 1C and Fig. S4B) in Bthal samples, with no difference in progenitors' composition (Fig. S4C). These results suggest that the Ery subsets deficit does not

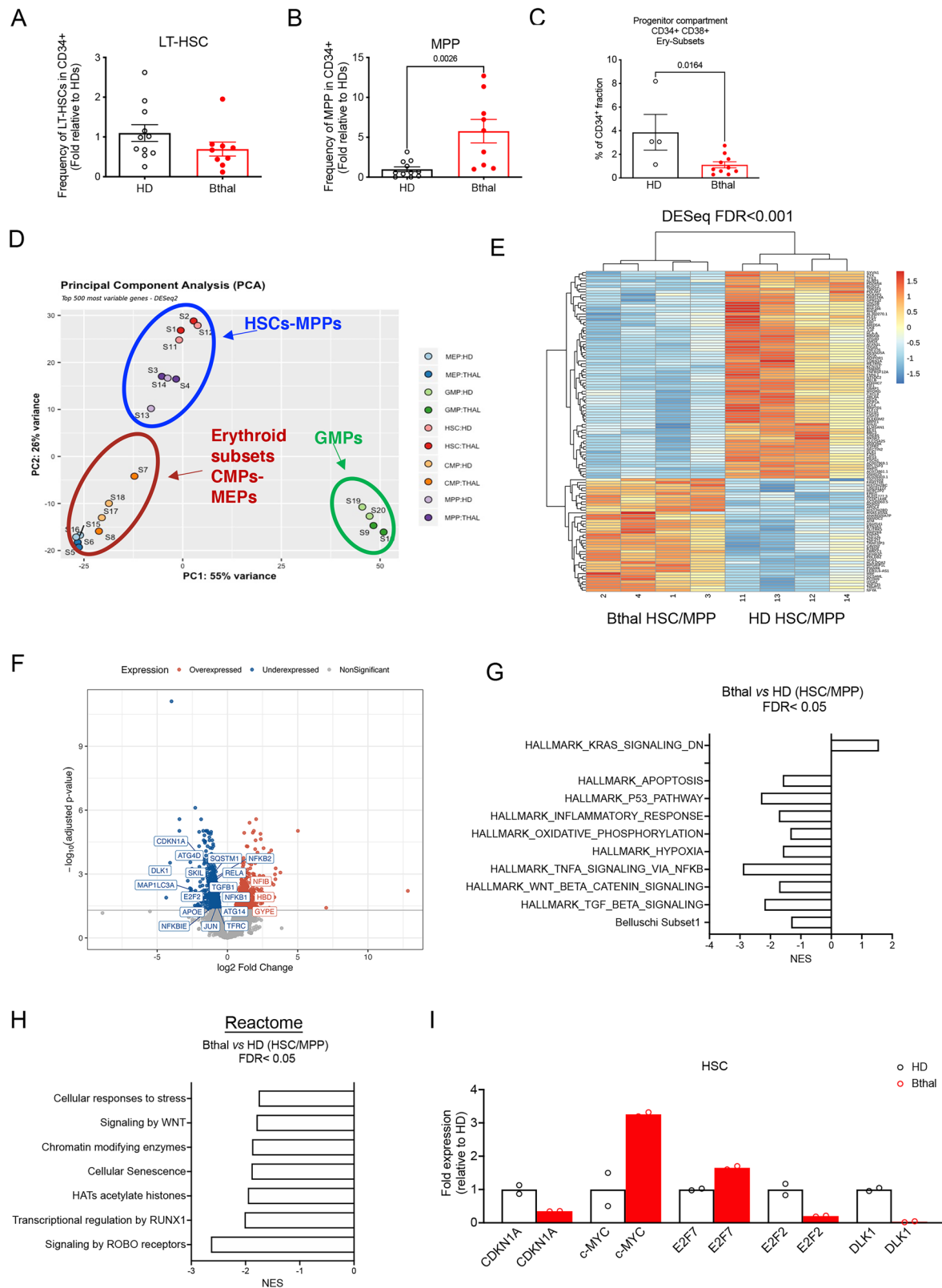
impoverish LT-HSCs since the continuous stimulus to erythroid cell production is acting at the level of the MPP population.

To profile transcriptional differences between Bthal and HD primitive hematopoietic cells, we sorted 5 distinct hematopoietic stem and progenitor cell (HSPC) subpopulations (HSCs, MPPs, CMPs, MEPs, GMPs) from BM CD34+ cells based on cell surface markers expression<sup>10</sup> and performed bulk RNAseq analysis. The CMP and MEP cells were further specifically enriched for Ery differentiation potential (Ery-CMP, Ery-MEP), defined as CMP F2/F3 and MEP F2/F3 fractions in ref. 10, based on the differential expression of CD71 and BAH1. Principal Component Analysis (PCA), performed using the 500 most variable Differentially Expressed Genes (DEGs), highlighted differences in cell compartments, irrespective of the Bthal or healthy source. PC1 separated GMP cells from the other subpopulations with a variance of 55%, thus suggesting that the other cell compartments were more transcriptionally related to each other than to this myeloid progenitor subset. Interestingly, PC2 gave rise to a separation of HSCs and MPPs that clustered very close to erythroid subsets, Ery-CMPs and Ery-MEPs (Fig. 1D).

We identified only 5 DEGs comparing HSCs and MPPs in HDs and 21 DEGs in Bthal samples (FDR < 0.05), by using EdgeR package (Supplementary Data 1). This transcriptional similarity was confirmed using the DESeq2 package (Supplementary Data 1) and it is in line with previously published data on cord blood-derived samples<sup>25</sup>. Thus, due to minor transcriptional differences, we considered HSC and MPP cells as a pool (HSC/MPP) for further analysis. Bthal HSC/MPPs were characterized by 92 or 116 DEGs compared to HD by using EdgeR or DESeq2 packages, respectively (FDR < 0.001) (Supplementary Data 1, Fig. 1E). Gene Ontology analysis (GO) highlighted that the 41 DEGs (FDR < 0.001) (Supplementary Data 2) upregulated in Bthal are involved in metabolic processes and proliferation, thus suggesting that these cells are cycling and more metabolically active compared to HD. Among genes with significantly lower expression in Bthal HSC/MPP, we identified negative regulators of cell cycle, such as *CDKN1A* (p21), genes involved in the regulation of maintenance of LT-HSC function and quiescence, as *DLK1*<sup>26</sup>, *TGFBI*<sup>27,28</sup>, autophagy<sup>15</sup>, and inflammatory genes<sup>29</sup> (Fig. 1F). On the other hand, genes positively associated to Mk and Ery differentiation, such as *NFIB*, *GPYE*, and *HBD* were over-expressed. Gene Set Enrichment Analysis (GSEA) using hallmark gene sets, showed that transcriptional pathways usually associated with HSC function, such as TGF $\beta$ , oxidative phosphorylation, TNF $\alpha$  via NF $\kappa$ B, inflammatory response, and hypoxia pathways, were downregulated ( $p < 0.05$ ) in Bthal, whereas a hallmark of DNA replication (KRAS signaling) was positively enriched (Fig. 1G, Supplementary Data 3). In addition, a gene signature specific for multilineage LT-HSCs (Subset1)<sup>11</sup> was negatively enriched in Bthal HSC/MPP (Fig. 1G, Supplementary Data 3). The reduced stemness features of Bthal HSC/MPP samples were corroborated by GSEA analysis using REACTOME database (FDR < 0.05), revealing a negative enrichment score in signaling by ROBO receptors<sup>30</sup> and by WNT<sup>31</sup>, as well as in cellular senescence (Fig. 1H, Supplementary Data 3). Finally, cell cycle genes were significantly deregulated in Bthal HSCs with high levels of *c-MYC*<sup>32</sup> and *E2F7*<sup>33</sup>, and low levels of *E2F2*<sup>34</sup> and *CDKN1A*<sup>35</sup> (Fig. 1I), suggesting that HSC/MPPs are likely more activated than their HD counterparts.

### Erythroid lineage priming of primitive hematopoietic cells in Bthal

The proportion of phenotypic Ery progenitors within the CD34<sup>+</sup> HSPC fraction was found altered in Bthal. Since HSC fate is coordinated by the expression of lineage factors, we analyzed the expression profile of Ery and Mk master regulators in HSCs and MPPs. Genes associated with Ery and Mk lineage specification as *NFE2*<sup>36</sup>, *NFIB*<sup>37</sup>, *GFI1B*<sup>38</sup>, and *KLF1*<sup>39</sup> (Fig. 2A, B) were highly expressed in Bthal HSCs and MPPs compared to the normal ones. Interestingly, *EPOR* expression is not affected in Bthal. An early Ery signature in Bthal HSC/MPPs was also confirmed by



performing deconvolution through the MuSiC algorithm<sup>40</sup> using single-cell transcriptomes from erythroid subpopulations<sup>41</sup>, as reference. The analysis revealed a higher estimated cell-type proportion of committed erythroid progenitor in Bthal samples compared to HD ones (Fig. S5), thus suggesting that Bthal HSCs/MPPs are endowed with an erythroid feature, leading them to a faster and earlier erythroid trajectory.

To investigate the origin of the unbalanced differentiation in Bthal patients, we evaluated the frequencies of rare multipotent cells (Ery/My/Ly Subset1) and cells with only My/Ly potential (Subset2), within the HSC/MPP pool and the CD49f+ HSC compartment (Fig. S6) using our recently identified novel markers<sup>11</sup>. The analysis revealed no statistically significant difference in these subsets in Bthal *vs* HD subjects (Fig. 2C, D).

**Fig. 1 | HSCs and MPPs characterization of bone marrow-derived CD34<sup>+</sup> cells from thalassemic patients.** **A** Frequencies of LT-HSCs within BM CD34<sup>+</sup> cells from Bthal patients, shown as fold relative to HD (HD  $n = 11$ ; Bthal  $n = 9$ ). mean  $\pm$  SEM is shown. **B** Frequencies of MPPs within BM CD34<sup>+</sup> cells from Bthal patients, shown as fold relative to HD (HD  $n = 11$ ; Bthal  $n = 9$ ).  $p$ -values by two-tailed unpaired  $t$ -test is shown; mean  $\pm$  SEM is shown. **C** Frequencies of Ery-enriched subsets in the progenitor compartment (CMP and MEP), identified using CD71 and BAH1 as markers, within BM CD34<sup>+</sup> cells from Bthal patients compared to HDs (HD  $n = 4$ ; Bthal  $n = 10$ ).  $p$ -values by two-tailed unpaired  $t$ -test is shown. mean  $\pm$  SEM is shown. **D** Principal Component Analysis (PCA) performed on the 500 most significant Differential Expression Genes (DEGs) in Bthal versus HD hematopoietic subpopulations, by

DESeq2 (HD  $n = 2$ ; Bthal  $n = 2$ ). **E** Heatmap of DEGs between Bthal and HD HSC/MPPs, by DESeq2, FDR < 0.001. **F** Volcano plot representation of DEGs in Bthal versus HD HSC/MPPs, by DESeq2, FDR < 0.05. **G** Gene Set Enrichment Analysis (GSEA) of categories from Hallmark MSigDB database in HSC/MPP pool of Bthal samples compared to HD, FDR < 0.05. Gene list of Subset1 (Ery/My/Ly) reported in Belluschi, S. et al.<sup>11</sup> was also evaluated. FDR < 0.05. NES, normalized enrichment score. **H** GSEA of categories from REACTOME database in HSC/MPP pool of Bthal samples compared to HD, FDR < 0.05. **I** Differentially expression of selected genes (normalized UMI counts) involved in HSC maintenance between Bthal (red bars) and HD HSCs (white bars), (HD  $n = 2$ ; Bthal  $n = 2$ ). Results are represented as Fold respect to Ctrl; mean  $\pm$  SEM is shown. Source data are provided as Source Data file.

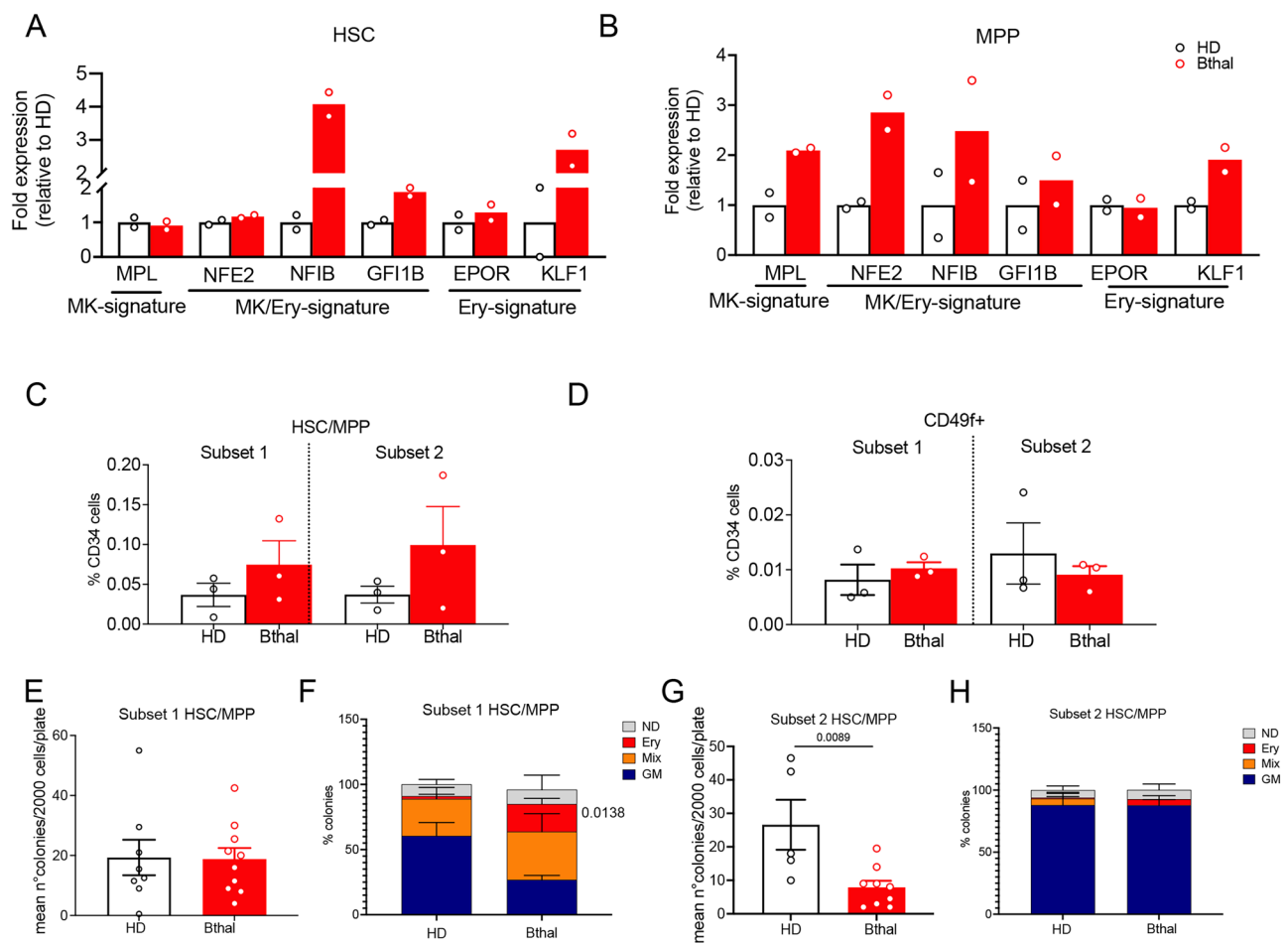


**Fig. 2 | Erythroid signature in primitive hematopoietic cells in Bthal.** Normalized UMI counts of selected erythroid-megakaryocytes genes differentially expressed between Bthal (red) and HD (grey), in HSCs (**A**) and MPPs (**B**) (HD  $n = 2$ ; Bthal  $n = 2$ ). Results are represented as Fold respect to Ctrl. mean  $\pm$  SEM is shown. **C** Frequencies of Subset1 and Subset2 within HSC/MPP pool in HD and Bthal samples (HD  $n = 3$ ; Bthal  $n = 3$ ). mean  $\pm$  SEM is shown. **D** Frequencies of Subset1 and Subset2 within HSC CD49f<sup>+</sup> cells in HD and Bthal samples (HD  $n = 3$ ; Bthal  $n = 3$ ). mean  $\pm$  SEM is shown. **E** Cloning efficiency of the HSC/MPP Subset 1 of Bthal samples compared to HD ones. Mean/number of colonies/2000 cells/plate (each dot represents the mean of 2 technical replicates) from Bthal and HD HSC/MPP Subset 1 of Bthal samples plated in a CFU assay ( $n = 8$  from HD  $n = 3$ ;  $n = 10$  from Bthal  $n = 3$ ). mean  $\pm$  SEM is shown. **F** Percentage of colonies generated by Bthal and HD HSC/MPP Subset1 and

containing differentiated cells (HD  $n = 3$ ; Bthal  $n = 3$ ). The type of colony: erythroid (E), granulocyte and myeloid (GM) or a combination of both (mix) is shown.  $P$ -value by two-tailed unpaired  $t$ -test; mean  $\pm$  SEM is shown. **G** Cloning efficiency of the HSC/MPP Subset 2 of Bthal samples compared to HD ones. Mean/number of colonies/2000 cells/plate (each dot represents the mean of 2 technical replicates) from Bthal and HD HSC/MPP Subset 2 of Bthal samples plated in a CFU assay ( $n = 5$  from HD  $n = 3$ ;  $n = 8$  from Bthal  $n = 3$ ).  $p$ -value by two-tailed unpaired  $t$ -test; mean  $\pm$  SEM is shown. **H** Percentage of colonies generated by Bthal and HD HSC/MPP Subset2 and containing differentiated cells (HD  $n = 3$ ; Bthal  $n = 3$ ). The type of colony: erythroid (E), granulocyte and myeloid (GM) or a combination of both (mix) is shown. mean  $\pm$  SEM is shown. Source data are provided as Source Data file.

Then, we evaluated the lineage potential of Subset1 and Subset 2 populations by plating sorted cells from HD and Bthal patients in semi-solid colony-forming unit (CFU) assay. The cloning efficiency of multipotent Subset1 was similar (Fig. 2E), but the type of differentiated colonies was distinctive, with more Ery-colonies (GlyA<sup>+</sup>), less

My-colonies (CD14<sup>+</sup> and/or CD15<sup>+</sup>), and a similar number of Mix colonies (CD14<sup>+</sup>/CD15<sup>+</sup> GlyA<sup>+</sup>) in Bthal patients (Fig. 2F). Conversely, the cloning efficiency of the bilineage Subset2 was significantly decreased in Bthal samples compared to HDs (Fig. 2G), while the type of colonies was similar (Fig. 2H). In summary, Bthal Subset1 produced

more colonies than Subset2 and generated cells with predominant Ery output. Thus, we can hypothesize that molecular changes occur early in Bthal hematopoietic cells driving them towards erythroid cell differentiation.

### HSC activation and accelerated Ery progenitor differentiation in Bthal patients

We next dissected the cellular composition and the molecular pathways of the early steps of hematopoiesis by performing scRNA-seq on BM CD34<sup>+</sup> cells and flow-sorted CD34<sup>+</sup> CD38<sup>-</sup> (CD45RA<sup>-</sup>) cells from Bthal patients ( $n = 6$ ) and age-matched pediatric HD ( $n = 4$ ). We also included in our analysis two previously published<sup>42</sup> pediatric BM scRNA-seq datasets (HD:  $n = 6$  total). After quality control, all samples were integrated with Seurat (v4), 36,878 cells were included into a UMAP embedding (Supplementary Data 4). These cells were annotated independently using two reference datasets<sup>24,43</sup>, (see methods; Fig. 3A, Fig. S7A–C). With both annotations (respectively named Zeng<sup>43</sup> and Mende<sup>24</sup>), we noted significant differences in HSPC composition of the CD34<sup>+</sup> HSPC compartment of Bthal patients compared to HD (Fig. 3B, Fig. S8A, B, Fig. S7D). Notably, the frequency of HSC/MPP populations was significantly higher (approximately 2-fold) in keeping with our phenotypic analysis. Bthal HSC/MPPs were also distributed differently within the HSC/MPP area (Fig. 3C), namely towards a less primitive area, marked by the expression of genes associated with HSC activation and lower expression of genes associated with HSC quiescence. Consistent with this, Bthal HSC/MPPs were significantly shifted downstream in pseudotime (Fig. 3D, Fig. S7E). Overall, these data indicate a relative increase in activated HSC/MPPs within the CD34<sup>+</sup> compartment of Bthal patients.

We next sought to characterize how the disease impacts gene expression within specific transcriptionally defined HSPC subsets. We therefore performed DESeq2 on pseudobulked populations from samples from the same batch (see Methods, Supplementary Data 5). We performed these comparisons independently in phenotypically purified HSC/MPPs (hereafter referred to as pheno HSC/MPPs) as well as in HSPC subsets annotated transcriptionally from CD34<sup>+</sup> (hereafter indicated by their respective cluster annotation). The largest number of transcriptional changes was found when comparing HSC/MPP subpopulations (Fig. S7F).

We next performed pathway analysis using GSEA (Supplementary Data 6, 7). The expression of a number of pathways such as TNF $\alpha$ /NF $\kappa$ B, interferon response and hypoxia was significantly downregulated in almost all HSPC subsets, including HSC/MPPs (Fig. 3E). This result was validated via ENRICH analysis of the genes differentially expressed in transcriptionally annotated HSC/MPPs (Supplementary Data 8). We also found that phenoHSC/MPPs and transcriptionally annotated Ery-biased MPPs significantly downregulated genes involved in TGF $\beta$  signaling (Fig. 3E). These results are consistent with the bulk RNAseq findings. In addition, E2F and Myc target genes, as well as G<sub>2</sub>/M checkpoint pathways were significantly enriched in Bthal Ery progenitor populations (from MEP to Ery) compared to HD (Fig. 3E). This is indicative of a higher proliferative status and accelerated erythropoiesis.

We next investigated lineage priming and differentiation trajectories of Bthal HSPCs. To this end, we first tested for enrichment of previously published signatures of stemness and lineage priming (Fig. 3F). HSC signatures, including one associated with dormancy<sup>1,25,44</sup>, were significantly downregulated in Bthal HSC/MPP subsets compared to HD, supporting the notion that Bthal HSC/MPPs are more activated than their HD counterparts. In contrast, MEP and Ery progenitors signatures were enriched in Bthal MEP and Ery progenitors compared to HD. Subset 1 HSC/MPPs were previously described as self-renewing HSC/MPPs with functionally verified erythroid potential<sup>11</sup>. Consistent with phenotypic Subset 1 HSC/MPPs being elevated in Bthal patients (Fig. 2C), Subset 1 HSC/MPPs signatures were significantly higher in

transcriptionally defined HSC/MPPs and MPP-MkEry of Bthal patients compared to HD (Suppl Fig. 7G). Finally, we performed GSEA pathway analysis comparing transcriptionally defined Subset 1 HSC/MPPs (Suppl Fig. 7H, see methods) in Bthal to those of HD and found enrichment of pathways highly similar to those enriched in HSC/MPPs (Fig. 3E).

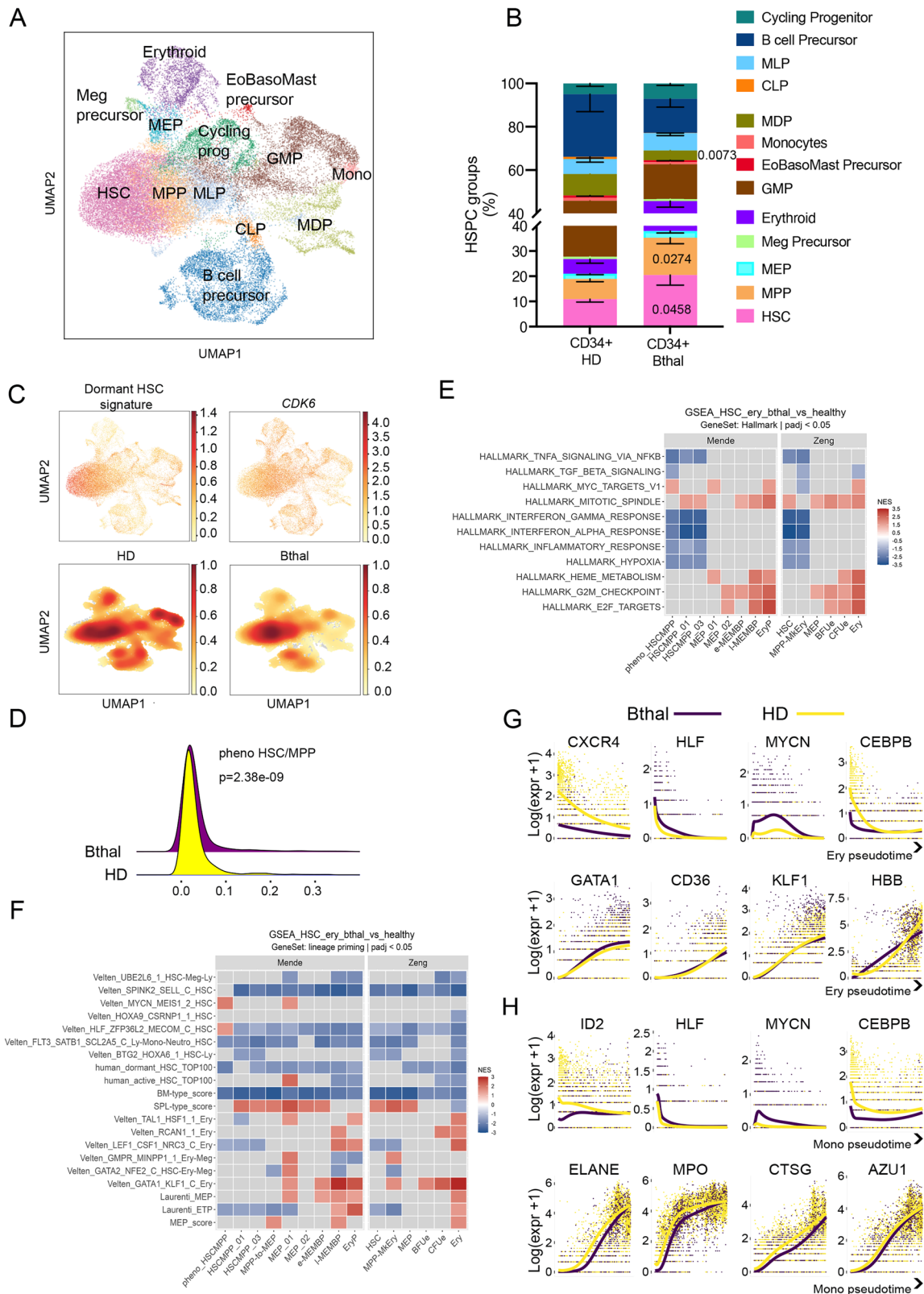
We next defined the trajectories of HSC differentiation towards the erythroid and myeloid lineages in Bthal patients and HD using CellRank<sup>45</sup>. We then employed tradeSeq<sup>46</sup> to perform trajectory-based differential expression analysis along the erythroid and myeloid trajectories, both initiating from the same single cell within the most primitive HSC/MPP\_01 cluster. We respectively found 706 and 719 differentially expressed genes between Bthal and HD along the erythroid (Ery) and monocytic (Mono) differentiation trajectories (Supplementary Data 9). 403 genes were differentially expressed in both trajectories and included genes related to stemness, which were either downregulated in Bthal from the most primitive HSCs (*ID2*, *CXCR4*, *AREG*) or upregulated in Bthal active MPPs (*MYCN*, *HLF*, Fig. 3G). Along the Ery trajectory, genes as *HBB* and *GATA1* were upregulated much earlier in Bthal than in HD HSPCs, and genes related to cellular damage remained more highly expressed throughout the whole trajectory (*DNAJBI*, *JUN*, Supplementary Data 9). Along the Mono trajectory, genes related to myeloid differentiation were downregulated throughout the time course or activated later (*MPO*, *CTSG*, *ELANE*, *AZUI*, Fig. 3H).

Altogether, these results indicate that in Bthal, the HSC/MPP compartment is activated, and its commitment is skewed towards erythropoiesis, with indications of sustained stress.

### TGF $\beta$ pathway drives the lineage commitment of Bthal HSCs towards erythroid lineage

To identify the molecular mechanisms driving the erythroid lineage choice of HSC in Bthal, we focused our studies on TGF $\beta$  pathway, because this pathway has an essential role in the maintenance of HSC self-renewal<sup>27</sup>, as well as in the erythropoietic process, with an opposing effect depending on the differentiation stage<sup>47</sup>. TGF $\beta$  pathway occurs through distinct routes (i.e., TGF $\beta$  signaling, BMP signaling) depending on the ligands and receptors involved<sup>48,49</sup>. Bulk RNAseq analysis showed that TGF $\beta$  signaling was downregulated in Bthal HSCs (Fig. 1G) with a lower expression of *ALK4* (*ACVR1B*), *ALK5* (TGF $\beta$  receptors of type I, *TGFBRI*), *TGFBRI2* (TGF $\beta$  receptors of type II) and the target genes *SKIL*<sup>50</sup> and *SMAD7*<sup>51</sup> compared with HD ones (Fig. 4A). Additionally, expression of two TGF $\beta$  signaling target genes, *CDKN1A* and *c-MYC*, was reduced and enhanced, respectively (Fig. 4A), implying that TGF $\beta$  signaling may be less active in Bthal HSCs than in HD ones. By contrast, BMP-type I (*ALK2*, *ALK6*) and II (*ACVR2B*) receptors, involved in the BMP signaling and positively regulating the erythropoietic process<sup>52</sup>, were overexpressed in Bthal HSCs (Fig. 4B).

TGF $\beta$  proteins are secreted by different cells in the body and in the BM niche, including HSC, acting in a paracrine or autocrine manner<sup>53</sup>. TGF $\beta$ 1 expressed and secreted by mesenchymal stromal cells (MSCs) can affect hematopoiesis<sup>54</sup>, and we recently demonstrated an impairment in the mesenchymal compartment of Bthal BM niche<sup>22</sup>. TGF $\beta$ 1 expression was reduced at the mRNA level in Bthal HSCs (Fig. 1F) and MSCs (Fig. 4C), as well as at the protein level in the BM plasma from Bthal patients (Fig. 4D). However, activin A, BMP2, and 4, involved in hematopoiesis<sup>55</sup> and lineage specification of HSCs<sup>56</sup>, were expressed at similar level in Bthal and HD MSCs (Fig. 4C). All these data suggest that a balance of the two signaling pathways is needed for correct HSC behavior. Despite the similar level of BMP molecules in MSCs, the reduced TGF $\beta$ 1 response in Bthal hematopoietic primitive cells might shift this balance towards the BMP signaling, with specific genes highly expressed, thus driving the cell fate towards the erythroid lineage.



It is known that TGFβ1 inhibits erythropoiesis not only at the level of early progenitors by reducing their reentry in the cell cycle, but also on intermediate and late erythroid progenitors by blocking their proliferation and accelerating their differentiation toward erythrocytes by skipping cell divisions<sup>47</sup>. Moreover, inhibition of TGFβ and activin signaling ameliorated ineffective erythropoiesis (IE) in myelodysplastic syndrome<sup>57</sup> and β-thalassemia<sup>58</sup>, respectively. Our

data showed that the expression of multiple TGFβ/BMP pathway components is altered in Bthal HSCs with an increased Ery colony-forming activity from purified Subset1 HSCs.

The role of the TGFβ/BMP pathway and the contribution by subset1 HSC/MPP in Ery-priming, have been assessed by the treatment of humanized mice NBSGW (NOD.Cg-Kit<sup>W-4J</sup>Tyr<sup>+</sup>Prkdc<sup>scid</sup>Il2rg<sup>tm1Wjl</sup>/ThomJ) with 10 mg/kg of TGFβ inhibitor (TGFβi) and/or 20 ng/g of BMP2

**Fig. 3 | Single cell landscape of CD34<sup>+</sup> differentiation in Bthal.** Analysis of 10x Genomics scRNA-seq from CD34<sup>+</sup> HSPCs and phenotypic HSC/MPP isolated from BM of Bthal patients or HD. **A** UMAP for 36,878 single cells from 6 Bthal patients and 6 HDs. Indicated lineage groups were derived from the conflation of clusters with similar cell identities annotated based on label transfer from Zeng et al.<sup>43</sup> (HSC, MPP, MEP, Meg precursors, MEP, Erythroid, EoBasoMast precursor, Cycling prog, GMP, Mono, MDP, MLP, CLP, B cell precursor). Original cluster annotation is shown in Fig. S7A. **B** Bar graph of the relative composition of HSPC groups shown in A in Bthal and HD. *P* values by two-tailed unpaired t-test; mean ± SEM is shown. **C** Top panels: UMAPs colored by the expression of a dormant HSC signature (left) and *CDK6* gene expression (right). Bottom panels: Gaussian kernel density

estimates plotted in the UMAP for HD (left) and Bthal (right) CD34<sup>+</sup> cells on UMAP. **D** Ridge plot of pseudotime values assigned to phenotypic HSC/MPPs of Bthal and HD. *P*-value by two-side Welsh t-test. Selected pathways **E** MSigDB hallmark, **F** published genesets related to stemness and lineage commitment) significantly enriched (*padj*<0.05) by GSEA in the populations indicated on the y axis. Red: enriched in Bthal; Blue: enriched in HD. A list of all enriched pathways is provided in Supplementary Data 6, 7. Terms with adjusted *p*-value (Benjamini-Hochber correction) less than 0.05 were considered significantly enriched. Representative examples of genes differentially expressed along the Ery (**G**) or monocytic (**H**) differentiation trajectory as identified by tradeSeq. Purple lines: Bthal; yellow lines: HD. Source data are provided as Source Data file.

molecule, known to act on early erythroid cell differentiation<sup>55</sup>. NBSGW mice were transplanted with human CD34<sup>+</sup> cells and treated with drugs at the 10th week, when successful humanization was achieved (Fig. 4E–G). Two weeks after treatment, the TGFβi-treated group of mice showed a lower frequency of CD49f<sup>+</sup> HSC (Fig. 4H) and, a reduction of Subset 2 (Fig. 4I). Conversely, no change in frequency was observed in Subset1 (Fig. 4J), thus resulting in a higher Subset1/Subset2 HSC/MPP ratio (Fig. 4K), compared with control and BMP2-treated mice. Moreover, repopulating human hematopoietic cells isolated from mice treated with TGFβi produced more erythroid colonies (Fig. 4L), thus indicating that blocking TGFβ signaling induces exhaustion of HSCs leading them to differentiate.

All these data support the hypothesis of the role of TGFβ signaling on Ery lineage differentiation in the HSC/MPP compartment.

To determine the molecular mechanism regulating lineage cell fate choice by the TGFβ/BMP axis, we investigated which target genes of these routes are involved. TGF-β and BMP signaling pathways have opposite effects on the expression of target genes<sup>59,60</sup>. Thus, we performed an in-silico analysis on a published dataset<sup>36</sup> by identifying genes carrying BMP-Responsive Element (BMP-RE) in Ery cells. We intersected this list of genes with the Bthal vs HD HSC/MPP DEG list. The analysis showed 119 BMP-RE target genes in Bthal DEGs (*padj*<0.01, Supplementary Data 10) and GO analysis revealed that these genes are involved in the macroautophagy pathway (Fig. 5A, Supplementary Data 11), which is the type of autophagy most related to cellular health and pathology<sup>61</sup>. Pre-ranked GSEA run on bulk RNAseq using as geneset the C5 subcollection from the MSigDB confirmed a negative enrichment of autophagic process in Bthal HSC/MPP (Fig. 5B). Among autophagy-related proteins, microtubule-associated protein1 *MAP1LC3B* (*LC3*) and the proteolytic enzyme *ATG4*, were down-regulated specifically in HSCs (Fig. 5C). Immunofluorescence staining showed a weaker and fewer, but still distinct and punctuated cytoplasmic staining of LC3 protein in Bthal LT-HSCs compared with HD ones (Fig. 5D–F), thus showing a reduced autophagic activity.

### Activation of autophagy restores the perturbed hematopoiesis

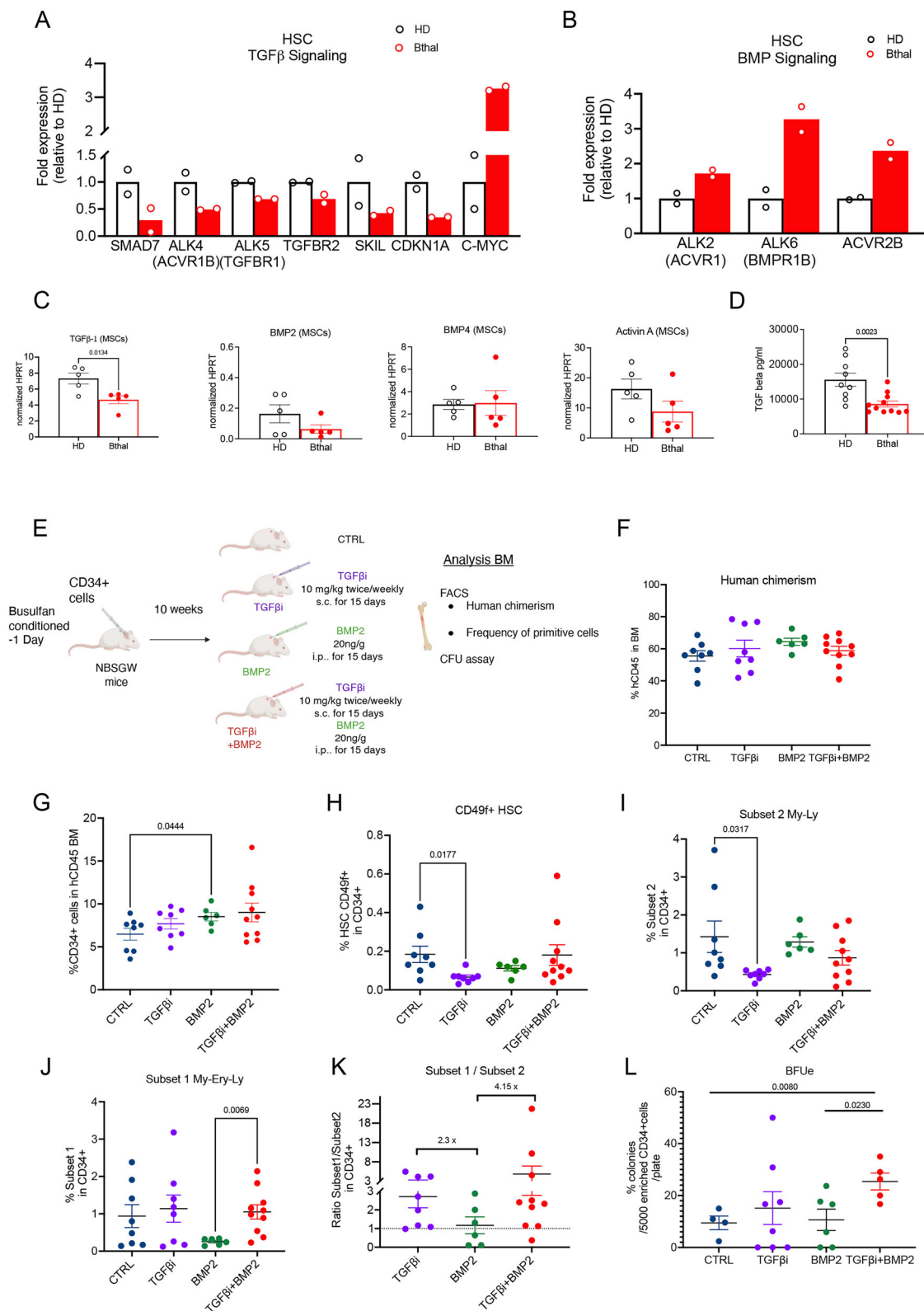
Our findings indicate that in Bthal patients the output of MPPs from primitive HSCs is imbalanced towards erythroid-biased MPPs. To better dissect the molecular mechanism, we used Bthal mice (*th3* strain)<sup>62</sup>, a mouse model of Bthal intermedia, which recapitulates the features of the pathology, such as severe anemia, impaired RBC morphology and hematological parameters, iron overload, and ineffective erythropoiesis. Flow-sorted HSCs from Bthal mice display an increased expression of erythroid transcription factor *Klf1*, and down-regulation of genes involved in the autophagic pathway and TGFβ signaling (Fig. 6A–C), thus mirroring the phenotype in patients. Accordingly, flow cytometry analysis revealed a reduction in the frequency of autophagic LT-HSCs in *th3* mice after Cyto-ID dye staining (Fig. 6D). Similarly to humans, no difference in the EpoR expression was observed. In addition, genes mainly involved in Mk cell differentiation, as *Mpl* and *Nfe2* resulted downregulated in Bthal mice supporting the hypothesis of HSC fate towards Ery lineage. Consistently, low amount

of TGFβ1 molecule was present in *th3* bone marrow fluid (Fig. 6E). Osteoblasts and stromal cells, which are defective in Bthal<sup>63</sup>, contributed to the low TGFβ production (Fig. S9).

Several studies reported that autophagy genes are also regulated by TGFβ signaling<sup>64–66</sup>. To test if the TGFβ signaling regulates the HSC cell fate towards erythroid lineage by reducing the HSC autophagic activity, we injected *wt* mice with 10 mg/kg of TGFβ inhibitor (TGFβi) (Fig. 6F). Thirty days after treatment, the frequencies of LT-HSCs and MPP<sup>Mk/E</sup> (megakaryocyte (Mk) and erythroid (E) lineage lineage-biased multipotent progenitors, Fig. S10A, B) resulted increased (Fig. 6G, H and Fig. S10B) along with an increased *Klf1* expression in LT-HSCs (Fig. 6I), master regulator of erythroid differentiation. In treated animals, we measured a reduction of LT-HSCs with autophagic activity by Cyto-ID dye staining and flow cytometry analysis (Fig. 6J and Fig. S10C) with a decreased *Map1lc3b* gene expression (Fig. 6K). In vitro treatment with TGFβ1 increased both the percentage of autophagic *th3* LT-HSCs and the autophagy level (Fig. 6L, M) by blocking their mTOR activity as shown by a decrease in pS6 expression (Fig. S10D, E). Strikingly, treatment with the autophagy inhibitor bafilomycin A further reduced the autophagic *th3* LT-HSCs. Overall, these data indicate that specific inhibition of TGFβ signaling in vivo leads to reduced autophagy in LT-HSCs and promotes their erythroid-biased differentiation.

Our data show that autophagy is regulated by TGFβ signaling through the expression of autophagic genes and the mTOR function. In cancer cells, TGFβ activates autophagy by decreasing the Ulk1 activity through mTOR<sup>66</sup> inhibition. To determine whether autophagic activity regulates the Ery lineage bias of HSCs through ULK1 protein, we studied the hematopoietic primitive compartment in the *Ulk1<sup>-/-</sup>th3/+* mouse model, in which the absence of ULK1 exacerbates the pathologic features of the disease<sup>67</sup>. Ery commitment of HSCs resulted in a decreased LT-HSC frequency and an increase of MPP<sup>Mk/E</sup> (Fig. 6N) together with a higher expression of *Klf1* in both populations (Fig. 6O, P). Thus, ULK1 deficiency in Bthal further depletes the hematopoietic compartment of primitive cells, promoting the HSC fate towards the Ery lineage.

Moreover, in vivo mTORC1 inhibition through systemic treatment of *th3* mice with rapamycin for 30 days restored the reduced content of LT-HSCs to normal levels (Fig. 7B and Fig. S11A). In the MPP compartment<sup>68</sup>, rapamycin increased the MPP<sup>Mk/E</sup> content (Fig. 7C and Fig. S11B) and *Klf1* expression level, which is higher in LT-HSC and MPP<sup>Mk/E</sup> in *th3* mice, is normalized (Fig. 7D, E). Rapamycin treatment induced an increase in the percentage of autophagic *th3* LT-HSCs and autophagy level (Fig. 7F, G) by blocking mTOR activity (Fig. 7H). As expected, treated mice exhibited an amelioration of anemia with an increase in RBC count and HBB level (Fig. S11C, D), as an effect of rapamycin on reducing free α-globin precipitates in erythroblasts<sup>67</sup>. In line with data obtained in mice, rapamycin treatment of Bthal Subset1 cells decreased their Ery cell output, without affecting the clonogenic potential (Fig. 7I, J), thus corroborating the role of autophagy in the modulation of erythroid commitment also in the human context.



## Discussion

In this work, we defined how the early steps of hematopoietic differentiation are altered in patients affected by transfusion-dependent Bthal, performing molecular and functional studies on recently identified HSC subpopulations and Ery progenitor subsets<sup>10,11</sup>. Our findings support a model wherein Bthal HSC lineage specification and differentiation are changed in the stressed BM microenvironment (Fig. 8). We show that in Bthal HSCs exit the quiescent state towards an

accelerated Ery differentiation. Paradoxically, we observed a relative depletion of Ery committed cells from the progenitor fraction compared to HD. We hypothesize this may arise from either MPP/progenitor cells with Ery potential quickly differentiating in response to niche signals, or from direct commitment towards erythroid precursors bypassing specific intermediate stages. The main drivers of this phenomenon are altered niche signals, linked to TGF $\beta$  pathway, together with the chronic state of anemia and its associated constant

**Fig. 4 | TGF $\beta$  inhibition induces erythroid priming of HSCs.** Normalized UMI counts of selected genes, involved in TGF $\beta$  (A) and BMP (B) signaling, differentially expressed between Bthal HSCs (red) and HD HSCs (white). Results are represented as Fold respect to Ctrl (HD  $n=2$ ; Bthal  $n=2$ ). mean  $\pm$  SEM is shown. C Transcribed level of molecules involved in TGF $\beta$  and BMP signaling evaluated by ddPCR in MSCs.  $P$  value by two-tailed unpaired t-test; mean  $\pm$  SEM is shown. D Evaluation of TGF $\beta$ 1 in Bthal and HD platelet-poor plasma by enzyme-linked immunosorbent assay (ELISA) (Bthal  $n=11$ ; HD  $n=9$ ).  $P$  value by two-tailed unpaired t-test; mean  $\pm$  SEM is shown. E Experimental plan for in vivo treatment of humanized mice with TGF $\beta$  inhibitor and/or BMP2. CD34 $^+$  mPB cells were administered to NBSGW female mice by retro-orbital injection. 9- to 10-week-old NBSGW mice were conditioned with busulfan injected intraperitoneally (15 mg/kg body weight) 24 h before transplantation. After 10 weeks, mice were treated with 10 mg/kg of TGF $\beta$  inhibitor (TGF $\beta$ i) by subcutaneous injection and/or 20 ng/g of BMP2 molecule by intraperitoneal injection, twice weekly for 2 weeks. Image was created with BioRender.com. (<https://BioRender.com/3tbmj37>). F Frequencies of hCD45 $^+$  in BM from untreated animals (ctrl  $n=8$ ) and after in vivo treatment with TGF $\beta$ i inhibitor ( $n=8$  mice), with BMP2 ( $n=6$  mice), or the combination of both (TGF $\beta$ i + BMP2  $n=10$  mice), from  $n=2$  independent experiments.  $P$ -values by two-tailed unpaired t-test; mean  $\pm$  SEM is shown. G Frequencies of CD34 $^+$  in hCD45 $^+$  BM from untreated animals (ctrl  $n=8$ ) and after in vivo treatment with TGF $\beta$ i inhibitor ( $n=8$  mice), with BMP2 ( $n=6$  mice), or the combination of both (TGF $\beta$ i + BMP2  $n=10$  mice), from

$n=2$  independent experiments.  $P$ -values by two-tailed unpaired t-test; mean  $\pm$  SEM is shown. H Frequencies of HSC CD49f $^+$  in hCD34 $^+$  from untreated animals (ctrl  $n=8$ ) and after in vivo treatment with TGF $\beta$ i inhibitor ( $n=8$  mice), with BMP2 ( $n=6$  mice), or the combination of both (TGF $\beta$ i + BMP2  $n=10$  mice), from  $n=2$  independent experiments.  $P$ -values by two-tailed unpaired t-test; mean  $\pm$  SEM is shown. I Frequencies of Subset2 in untreated animals (ctrl  $n=8$ ) and after in vivo treatment with TGF $\beta$ i inhibitor ( $n=8$  mice), with BMP2 ( $n=6$  mice), or the combination of both (TGF $\beta$ i + BMP2  $n=10$  mice), from  $n=2$  independent experiments.  $P$ -values by two-tailed unpaired t-test; mean  $\pm$  SEM is shown. J Frequencies of Subset 1 in untreated animals (ctrl  $n=8$ ) and after in vivo treatment with TGF $\beta$ i inhibitor ( $n=8$  mice), with BMP2 ( $n=6$  mice), or the combination of both (TGF $\beta$ i + BMP2  $n=10$  mice), from  $n=2$  independent experiments.  $P$ -values by two-tailed unpaired t-test; mean  $\pm$  SEM is shown. K Subset1/Subset2 ratio in all groups of treated mice relative to untreated ones. Group of mice: TGF $\beta$ i inhibitor ( $n=8$  mice), with BMP2 ( $n=6$  mice), or the combination of both (TGF $\beta$ i + BMP2  $n=10$  mice), from  $n=2$  independent experiments.  $P$ -values by two-tailed unpaired t-test; mean  $\pm$  SEM is shown. L Colony assay on CD34 $^+$  cells purified from the untreated and treated animals. The percentage of BFUe colonies is shown. Each dot represents the mean of two dishes/mouse. Untreated animals (ctrl  $n=4$ ), TGF $\beta$ i inhibitor ( $n=8$ ), BMP2 ( $n=6$ ), or the combination of both (TGF $\beta$ i + BMP2  $n=5$ ), from  $n=2$  independent experiments.  $P$ -values by two-tailed unpaired t-test; mean  $\pm$  SEM is shown. Source data are provided as a Source Data file.

BM stimulation to produce RBCs. We found that the low level of TGF $\beta$ 1, produced by MSCs and OBs, enhanced the Ery commitment of HSC, while reducing their autophagic activity.

Overall, our findings support the concept of an adaptive model of hematopoiesis, shaped in response to a disease-specific cellular deficit and altered BM microenvironment. First, we reported an alteration in Bthal BM primitive compartment with an increase in the MPP frequency and a reduction of the Ery/Mk-enriched subsets in the progenitor compartment. Transcriptome profile, from bulk RNAseq and scRNAseq, highlighted that Bthal HSC/MPPs are in an active state. Specific pathways contributing to maintain a quiescent state, such as TGF $\beta$ , TNF $\alpha$ , and hypoxia pathway, were deregulated along with Subset1-specific genes<sup>11</sup>, suggesting a reduced long-term repopulating potential and a faster kinetics of quiescence exit as marked by an enrichment of transcription and splicing processes in Bthal HSC cluster and high CDK6 expression<sup>69</sup>. scRNAseq data revealed that human Bthal HSC/MPP subsets display a low degree of dormancy<sup>44</sup>, indicating a reduced quiescence of HSCs as we previously showed by in vivo a label-retaining assay<sup>23</sup>. In addition, high c-MYC expression in Bthal HSCs could contribute to an exhaustion of the LT-HSC pool, enhancing the differentiation at the expense of self-renewal<sup>32</sup>. Consistently, genes involved in cell cycle regulation, such as *E2F2* and *CDKN1A*(p21) are downregulated. *E2F2* is an activator of G1/S transition, and it is degraded during late S-G2 phases<sup>34</sup>, while p21 is implicated in the maintenance of quiescence<sup>70</sup>.

Accordingly, our previous data reported that Bthal HSCs accumulate in S phase, because of the reduction of G1 phase<sup>23</sup>. Moreover, we discovered enhanced functionally biased HSCs towards erythroid lineage, corroborated by the upregulation of genes specifically involved in the transition from HSCs to MPPs and in the differentiation towards Mk and Ery lineage<sup>10,39,71</sup> (*NF1B*, *GFI1B*, *KLF1*, *NFE2*), thus promoting Ery progenitors to accelerate in their differentiation process, as highlighted by scRNAseq data. This condition is likely driven by an increase in erythroblast proliferation due to ineffective erythropoiesis. Trajectory analysis revealed a different transcriptional dynamic across hematopoiesis in Bthal. The HSC compartment displays low expression of genes associated with primitive HSCs (low *ID2*, *CXCR4*, *AREG*). Instead, we observed an expanded compartment of activated MPPs with high levels of *MYCN* and *HLF* expression, endowed with an increased erythroid and reduced monocytic priming. Accordingly, we observed early expression of erythroid-specific genes

(i.e., *HBB*, *GATA1*) in the erythroid differentiation trajectory and a delay in the expression of monocytic genes in the myeloid one.

The TGF $\beta$  pathway is involved in the maintenance of HSC self-renewal<sup>27</sup>, and controls the erythropoietic process, with a distinct effect based on the stage of maturation<sup>47</sup>. TGF $\beta$  signaling occurs through distinct routes depending on the ligands and receptors involved<sup>48,49</sup>. Among TGF $\beta$  family members, TGF $\beta$ 1 molecule preserves the quiescent state of HSCs<sup>72,73</sup> and suppresses cell cycle progression by reducing c-MYC levels, increasing p21 expression<sup>74,75</sup>. Low concentrations of TGF $\beta$  have been shown to drive differentiation towards the myeloid fate in a dose-dependent manner<sup>76</sup>. Thus, we propose that low levels of TGF $\beta$ 1 in Bthal, induce a higher c-MYC expression and suppress the expression of p21, pushing HSC away from the quiescent state towards differentiation. In vivo treatment of humanized mice showed a reduction of HSC pool size with the increase of their erythroid differentiation potential only after treatment with the inhibitor of TGF $\beta$  signaling, corroborating our hypothesis of the role TGF $\beta$  signaling in promoting HSCs to differentiate. In the mouse model, the TGF $\beta$ i treatment increases the frequency of LT-HSCs, at the time of analysis, probably inducing them to exit from the quiescence state, proliferate, and differentiate, as demonstrated by an increase of the erythroid transcription factor *Klf1*.

Interestingly, TGF $\beta$  signaling, through TGF $\beta$  and Activin, known negative regulators of erythropoiesis, leads to the acceleration of Ery progenitor differentiation<sup>47</sup>. On the contrary, the BMP-SMAD signaling is a positive regulator of the erythropoietic process, involved in the expansion of stress BFU-E<sup>52,77</sup>. In line with this, our data showed the downregulation of TGF $\beta$  signaling in Bthal HSC along with an upregulation of *ALK2* (*ACVRI*), *ALK6* (*BMPRIIB*), *ACV2B*, specifically involved in BMP-SMAD pathway, known to regulate both hematopoiesis and erythropoiesis.

We recently reported impaired Bthal HSC function due to the altered interaction with stroma and osteolineage cells in *th3* mice<sup>23,63</sup> and the poor HSC supporting capacity of the BM stroma in Bthal patients<sup>22</sup>. In the context of this altered BM niche, here we further showed that the production of TGF $\beta$ 1 by HSCs and MSCs is reduced, with a potential autocrine effect on their functions. TGF $\beta$  dysregulation affects MSC fate, uncoupling bone remodeling and leading to skeletal disorders<sup>78</sup> and, indeed defective *th3* OBs showed a low TGF $\beta$ 1 mRNA expression. In line with our data, Valletta et al.<sup>79</sup> have recently shown that in aged murine BM stroma, blocking TGFBR1 signaling impaired the HSC quiescent state and function, and increased the

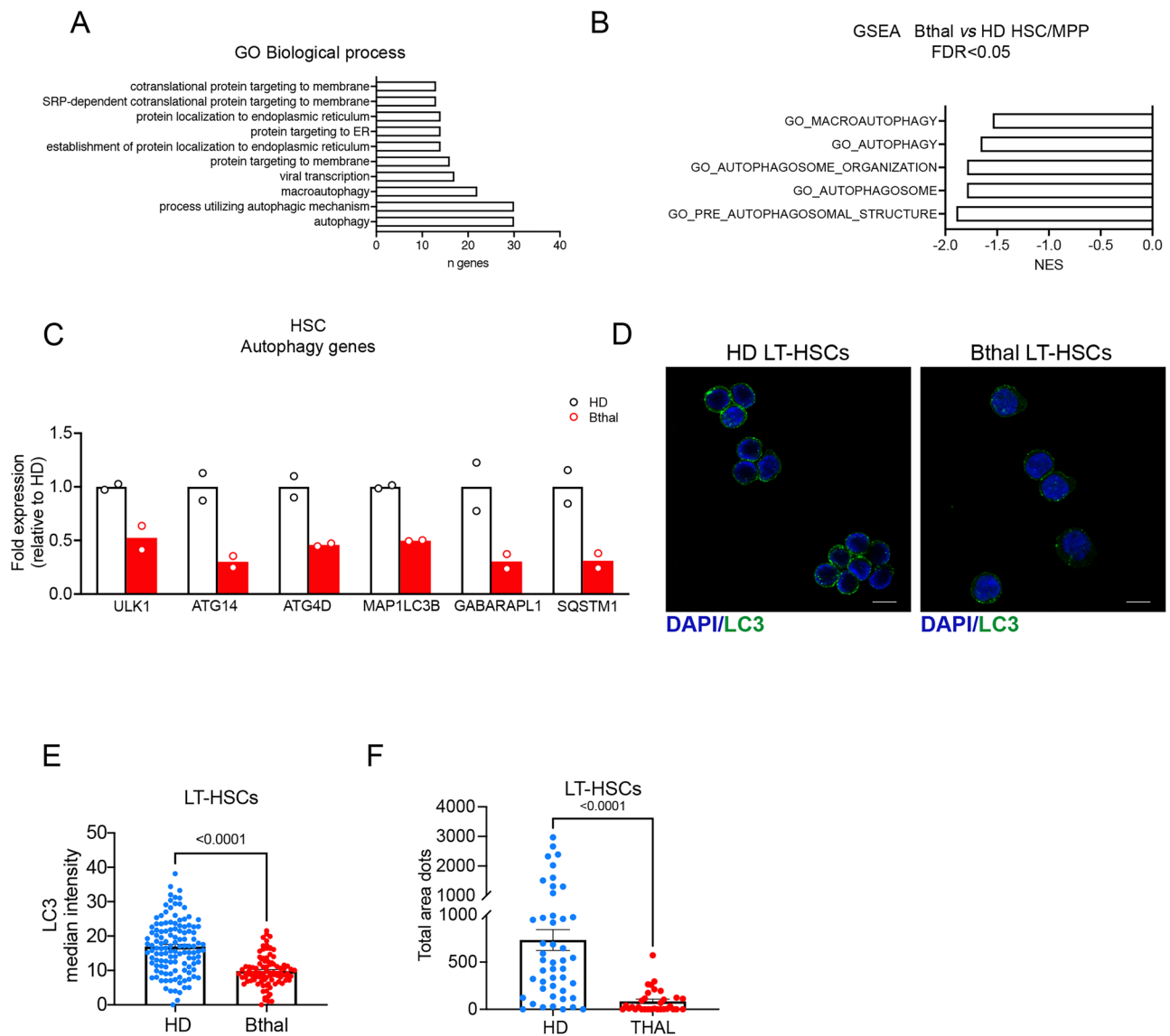


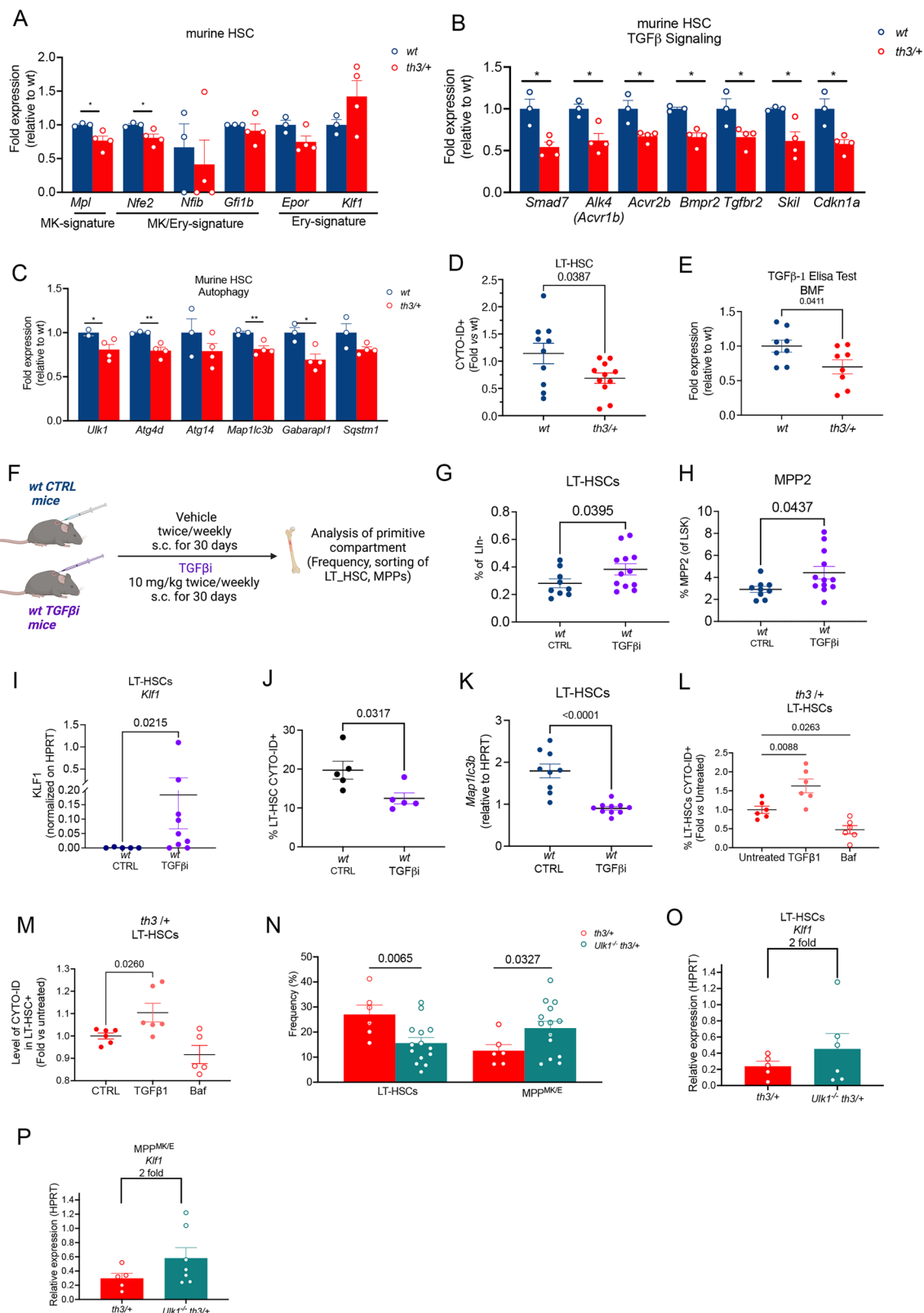
**Fig. 5 | Autophagy is reduced in Bthal LT-HSCs.** **A** DEGs carrying BMP responsive element (BMP-RE) between Bthal and HD HSC/MPP. Gene Ontology (GO) analysis of 120 target genes of BMP pathways,  $\text{padj} < 0.01$ . Terms with adjusted p-value (Benjamini-Hochber correction). **B** GSEA of categories from MSigDB database in HSC/MPP pool of Bthal samples compared to HD,  $\text{FDR} < 0.05$ . **C** Genes of autophagy deregulated in Bthal HSC. Normalized UMI counts of selected genes, involved in Autophagy, differentially expressed between Bthal HSCs (red) and HD HSCs (white). Results are represented as Fold respect to Ctrl (HD  $n = 2$ ; Bthal  $n = 2$ ).

**D** Representative microscopy images of DAPI (blue) and LC3 staining (green) of purified HD and Bthal sorted LT-HSCs. Scale bar 10  $\mu\text{m}$ .  $n = 3$  independent experiments ( $n = 3$  HD samples and  $n = 3$  Bthal samples). **E** Quantification of LC3 median intensity of evaluated foci in HD and Bthal LT-HSCs (HD  $n = 3$ ; Bthal  $n = 3$ ). About total 100 nuclei were analyzed for condition.  $P$ -values by two-tailed unpaired t-test; mean  $\pm$  SEM. **F** the area of evaluated foci in HD and Bthal LT-HSCs (46 nuclei from HD  $n = 3$ ; 32 nuclei from Bthal  $n = 3$ ).  $P$ -values by two-tailed unpaired t-test; mean  $\pm$  SEM. Source data are provided as Source Data file.

erythroid progenitor output<sup>79</sup>. Overall, our results indicate that the reduced TGF $\beta$  stimulation affects the Bthal HSC pool driving its enhanced erythroid commitment.

To determine the molecular mechanism regulating lineage cell commitment by the TGF $\beta$  pathway, we investigated which target genes of this route are involved. TGF- $\beta$  and BMP molecules regulate the expression of the same target genes with opposing effects<sup>59,60</sup>. In silico analysis of published data sets<sup>36</sup> revealed that genes carrying BMP-RE and involved in the autophagic process, were downregulated in Bthal HSCs. Our in vivo data suggest that TGF $\beta$  and not BMP signaling has a major role in driving erythroid priming of HSC. Since TGF $\beta$  activates autophagy by upregulating *ATG* genes<sup>64</sup> and *ULK1*<sup>66</sup> or by impeding *mTOR*<sup>65</sup>, the reduced TGF $\beta$  response in Bthal could be insufficient to induce proper levels of autophagy, an essential mechanism for lineage-biased commitment<sup>80,81</sup>. Mitochondrial autophagy, through the *NIX*

receptor, is an important mechanism for the maturation of erythroid cells<sup>82</sup>. Thus, we cannot exclude an impaired mitophagy in Bthal HSCs. The alteration of autophagy was corroborated experimentally by showing reduced autophagic activity and expression of LC3 protein in Bthal LT-HSCs. In vivo inhibition of TGF $\beta$  route reduces the percentage of LT-HSCs with autophagic activity, the *Map1lc3* expression, and increases the expression of *Klf1*, a master regulator of erythropoiesis. The addition of TGF $\beta$ 1 restores the autophagy levels in *th3* LT-HSCs by blocking mTOR activity, as reported in cancer cells<sup>66</sup>. The complete loss of *Ulk1* further reduces LT-HSC frequency with an increase in their erythroid signature, suggesting that the Ery lineage bias of HSCs is controlled by their autophagic activity. Systemic in vivo treatment with mTOR inhibitor can restore not only the frequency of LT-HSCs in *th3/+* mice and the autophagy but also the normal transcript levels of *Klf1*, thus normalizing the HSC pool by reducing their enhanced



commitment. The molecular effect of rapamycin is also evident on MPP<sup>MK/E</sup>, although they result expanded at the time of analysis. The biological response in MPP<sup>MK/E</sup> could be slower than in HSCs, or we cannot exclude that the low *Klf1* level can drive only a fraction towards the My lineage, at least in the murine system.

In normal mice, EPO drives the differentiation trajectory of the erythroid lineage from MPPs<sup>41</sup>, and inflammatory signals, such as IL17A,

enhance this response<sup>41</sup>. High EPO levels in Bthal might further prime HSCs towards Ery fate. Differently, we found that EPOR expression and Epo-mediated signaling pathway are not altered in Bthal HSC and MPP, both in humans and mice, thus suggesting that Epo is not the major driver. In addition, we cannot exclude that signals of sterile inflammation can also contribute to the Bthal model of hematopoiesis since inflammatory response is deregulated in Bthal HSC/MPPs and along

**Fig. 6 | TGF $\beta$  inhibition induces a reduction of autophagic activity.**

**A** Normalized UMI counts of selected genes, differentially expressed between th3/+ HSCs (red) and wt HSCs (blue) purified by FACS<sup>23</sup>. Results are represented as Fold respect to wt (th3/+  $n = 3$ ; wt  $n = 4$ ). \* $p < 0.05$ , \*\* $p < 0.01$ , by two-tailed unpaired t-test; mean  $\pm$  SEM is shown. **B** Normalized UMI counts of selected genes, involved in TGF $\beta$  signaling, differentially expressed between th3/+ HSCs (red) and wt HSCs (blue)<sup>23</sup>. Results are represented as Fold respect to wt (th3/+  $n = 3$ ; wt  $n = 4$ ). \* $p < 0.05$ , \*\* $p < 0.01$ , by two-tailed unpaired t-test; mean  $\pm$  SEM is shown. **C** Normalized UMI counts of selected genes, involved in autophagy pathway, differentially expressed between th3/+ HSCs (red) and wt HSCs (blue)<sup>23</sup>. Results are represented as Fold respect to wt. (th3/+  $n = 3$ ; wt  $n = 4$ ). \* $p < 0.05$ , \*\* $p < 0.01$ , by two-tailed unpaired t-test; mean  $\pm$  SEM is shown. **D** Percentage of Cyto-ID<sup>+</sup> in LT-HSCs in wt ( $n = 10$ ) and treated th3/+ mice ( $n = 11$ ) from  $n = 2$  independent experiments.  $p$ -value by two-tailed unpaired t-test; mean  $\pm$  SEM is shown. **E** Evaluation of TGF $\beta$ 1 in th3/+ and wt BM fluid by ELISA (wt  $n = 8$ ; th3/+  $n = 8$ ).  $p$ -value by two-tailed unpaired t-test; mean  $\pm$  SEM is shown. **F** Experimental plan for in vivo treatment of wt mice with TGF $\beta$  inhibitor. Image created with BioRender.com. (<https://BioRender.com/ho2ypan>). **G** Frequencies of LT-HSCs in untreated animals (ctrl  $n = 9$ ) and after in vivo treatment with TGF $\beta$  inhibitor ( $n = 12$ ), from  $n = 2$  independent experiments;  $p$ -value by one-tailed unpaired t-test; mean  $\pm$  SEM is shown. **H** Frequencies of MPP<sup>Mk/E</sup> (in untreated animals (ctrl  $n = 9$ ) and after in vivo treatment with TGF $\beta$  inhibitor ( $n = 12$ ), from  $n = 2$  independent experiments;  $p$ -value by two-tailed unpaired t-test; mean  $\pm$  SEM is shown. **I** *Klf1* expression measured on sorted LT-HSCs from ctrl ( $n = 5$ ) and treated wt mice ( $n = 9$ ) from  $n = 3$  independent

experiment.  $p$ -value by Mann-Whitney test; mean  $\pm$  SEM is shown. **J** Percentage of Cyto-ID<sup>+</sup> in LT-HSCs in ctrl wt ( $n = 5$ ) and treated wt mice ( $n = 5$ ).  $p$ -value by Mann-Whitney test. mean  $\pm$  SEM is shown. **K** *Map1lc3b* gene expression measured on sorted LT-HSCs from ctrl ( $n = 9$ ) and treated wt mice ( $n = 10$ ).  $p < 0.0001$  by two-tailed unpaired t-test; mean  $\pm$  SEM is shown. The percentage of Cyto-ID<sup>+</sup> in LT-HSCs (**L**) in untreated ( $n = 6$ ) and after in vitro treatment of th3/+ LT-HSCs with TGF $\beta$ 1 molecule ( $n = 6$  samples) or Bafilomycin A ( $n = 6$  samples), as control. Each sample is a pool of 4-6 mice. ( $n = 3$  independent experiments).  $p$ -values by one-way ANOVA, with Dunnett's multiple comparison test. Mean  $\pm$  SEM is shown. **M** Quantification of Cyto-ID level dye levels (MFI) in untreated ( $n = 6$  samples) and after in vitro treatment of th3/+ LT-HSCs with TGF $\beta$ 1 molecule ( $n = 6$  samples) or Bafilomycin A ( $n = 5$  samples), as control. Values are shown as fold versus the untreated one.  $p$ -value by Mann-Whitney test. mean  $\pm$  SEM is shown. **N** Frequencies of LT-HSCs, MPP<sup>Mk/E</sup> in HSPC at 12–20 weeks after transplantation from th3/+ ( $n = 5$ ) and *Ulk1*<sup>-/-</sup> th3/+ ( $n = 6$ ) mice from  $n = 2$  independent experiments  $P$ -values by two-tailed unpaired t-test; mean  $\pm$  SEM is shown. **O** Gene expression of *Klf1* was measured on sorted LT-HSCs from th3/+ ( $n = 5$ ) and *Ulk1*<sup>-/-</sup> th3/+ ( $n = 6$ ) mice from  $n = 2$  independent experiments. Relative expression on HPRT. th3/+, red; *Ulk1*<sup>-/-</sup> th3/+ green. Two-tailed unpaired t-test; mean  $\pm$  SEM is shown. **P** Gene expression of *Klf1* was measured on sorted MPP<sup>Mk/E</sup> (P from th3/+ ( $n = 5$ ) and *Ulk1*<sup>-/-</sup> th3/+ ( $n = 6$ ) mice from  $n = 2$  independent experiments. Relative expression on HPRT. th3/+, red; *Ulk1*<sup>-/-</sup> th3/+ green. Two-tailed unpaired t-test; mean  $\pm$  SEM is shown. Source data are provided as Source Data file.

the Ery trajectory. In recent years, many studies have demonstrated that inflammatory cytokines, like IL1 $\beta$ , TNF $\alpha$ , IFN $\alpha$ , are able to directly affect HSC differentiation and function<sup>68,83–85</sup>. Preliminary data highlighted a role of TNF $\alpha$  via NF- $\kappa$ B signaling on HSC cell lineage fate in Bthal (Chianella G. et al, manuscript in preparation). Understanding how HSC commitment is regulated and shaped in response to specific clues dictated by the Bthal condition, paves the way for a deeper knowledge of the pathophysiology and optimization of the therapeutic interventions in this complex common disease.

## Methods

### Our research complies with all relevant ethical regulations

**Human samples.** Human CD34<sup>+</sup> samples used in this study are listed in Supplementary Data 12. Samples were collected upon informed consent in accordance with the Helsinki Declaration and with local ethical committee approvals. Healthy donors (HD) BM-derived CD34<sup>+</sup> cells were purchased from Lonza (Basel, Switzerland). Mobilized-Plerixafor cells from HD were purchased from ALLCELLS (Alameda, CA, USA) or Stemexpress (Folsom, CA, USA). BM and mobilized cells from patients affected by transfusion-dependent  $\beta$ -thalassemia were obtained in the context of pre-transplantation evaluation for allogeneic BMT, or Phase II clinical trial of mobilization (EudraCT #2011-000973-30) or TIGET-BTHAL phase 1/2 clinical study (NCT02453477) after obtaining patient or parental informed consent and were approved by San Raffaele Scientific Institute Ethical Committee. Healthy pediatric samples (UK) were collected with Research Ethics Committee (REC) approval 12/LO/0426. Human MSCs from HD and Bthal BM aspirates were described in<sup>22</sup>.

**Mice.** Male and female C57BL/6 wild-type (*wt*) mice were purchased from Charles River. C57BL6/Hbbth3/+ (*th3*) mice were purchased from The Jackson Laboratory and bred to maintain the colony in heterozygosity. All animal experiments were performed in accordance with approved protocols of the Institutional Animal Care and Use Committees of San Raffaele Institute (IACUC n°1315). All the analyses were performed on adult 12- to 14-week-old mice, unless differently specified.

To evaluate the effect of TGF $\beta$  inhibitor in vivo, wt mice were treated with Reblozyl<sup>®</sup> (Bristol Myers Squibb) by subcutaneously injection (10 mg/kg) twice weekly for 4 weeks<sup>86</sup>. To assess the effects of Rapamycin, 12-week-old mice were treated with Rapamycin (Cat.

15424849, ThermoScientific) intraperitoneally (4 mg/kg daily) or vehicle (sirolimus vehicle; 0.5% ethanol, 5% Tween 80, and 5% polyethylene glycol 400) for 30 days before cell sorting and phenotypic analysis was performed. For studies in *Ulk1*<sup>-/-</sup> *th3* mice, the mice were generated with fetal liver cells from embryos of different genotypes as described in ref. 67. Briefly, 8-week-old C57BL/6 CD45.1 recipient mice were lethally irradiated (with 11.25 Gy); after a 24-h interval, they received a transplant of  $2 \times 10^6$  fetal liver cells from CD45.2 E14.5 embryo donors (*Ulk1*<sup>-/-</sup> *th3*, *th3*) via tail vein injection. Experimental protocols were approved by the Institutional Animal Care and Use Committee at St. Jude Children's Research Hospital. Peripheral blood from mice was collected into lithium heparin-coated microvettes (Sarstedt). All blood parameters were measured using a Hemocytometer Procyte DX.

For xenotransplantation in vivo studies,  $7 \times 10^5$  of CD34<sup>+</sup> mPB cells were administered to NOD.Cg-Kit<sup>W-4J</sup> Tyr Prkdc<sup>scid</sup> Il2rg<sup>tm1Wjl</sup>/ThomJ (NBSGW) (Jackson Laboratory) by retro-orbital injection. After 10 weeks, mice were treated with 10 mg/kg of Reblozyl<sup>®</sup> (Bristol Myers Squibb) (TGF $\beta$  inhibitor, TGF $\beta$ ) by subcutaneously injection<sup>86</sup> and/or 20 ng/g of BMP2 molecule (PEPROTECH) by intraperitoneal injection<sup>87</sup>, twice weekly for 2 weeks. Mice were maintained in a specific pathogen-free animal facility. Procedures were performed according to protocols approved by the Committee for Animal Care and Use of San Raffaele Scientific Institute. 9- to 10-week-old NBSGW female mice were conditioned with busulfan (Sigma-Aldrich) injected intraperitoneally (15 mg/kg body weight) 24 h before transplantation to provide partial depletion of murine BM cells, allowing high engraftment of human cells.

**Sample preparation for flow cytometry sorting and analysis.** To separate different cell populations from human CD34. Moreover, in vivo mTORC1 inhibition through cells, cells were first thawed by dropwise addition of MACS Buffer supplemented with BSA and EDTA (Miltenyi Biotech) and then incubated for 30 min in the dark at 4 °C in MACS Buffer supplemented with BSA and EDTA antibody mix. Depending on the experiment, cells were stained with antibody panels A, B, C, or D.

Murine total BM cells were obtained by flushing femurs and tibiae. To analyze primitive progenitor and stem cell populations lineage depletion was performed to enrich for lineage negative (Lin-) cells, using lineage-specific antibodies (GRI, CD11b, CD45R/B220, CD3, TER-

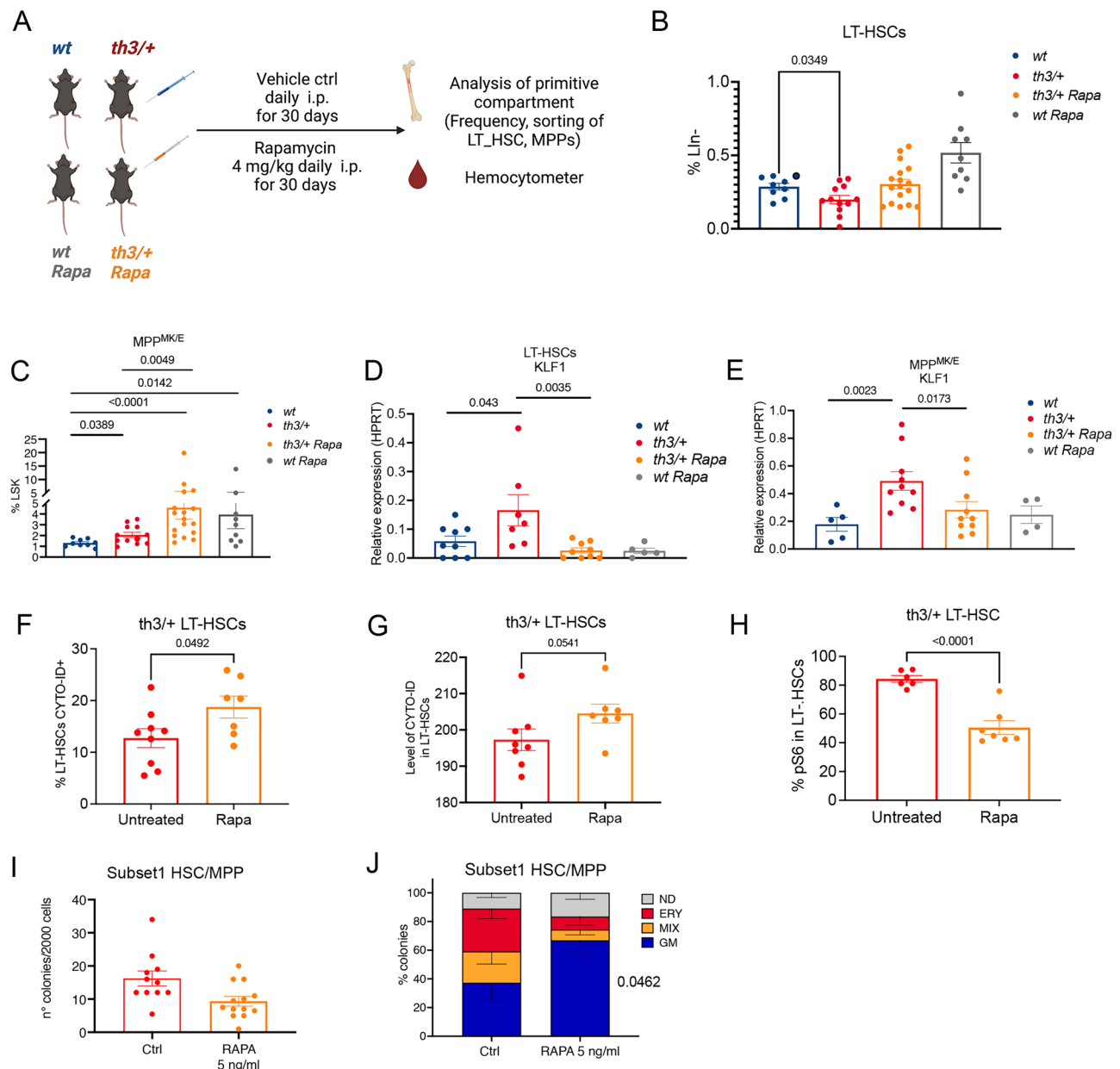


**Fig. 7 | mTOR inhibition restores the unbalanced hematopoiesis in Bthal.**

**A** Experimental plan for in vivo treatment of wt and *th3/+* mice with rapamycin 4 mg/kg i.p. Image created with Biorender. (<https://BioRender.com/qlii427>).

**B** Frequencies of HSC in untreated animals and after in vivo treatment with mTOR inhibitor rapamycin. wt ( $n = 9$ ) mice, blue; *th3/+* ( $n = 12$ ) mice, red; *th3/+* Rapa ( $n = 17$ ) mice, wt Rapa ( $n = 9$ ) mice from 3 independent experiments.  $p$ -values by Mann-Whitney test; mean  $\pm$  SEM is shown.

**C** Frequencies of  $MPP^{MK/E}$  in untreated animals and after in vivo treatment with mTOR inhibitor rapamycin. wt ( $n = 9$ ) mice, blue; *th3/+* ( $n = 12$ ) mice, red; *th3/+* Rapa ( $n = 17$ ) mice, wt Rapa ( $n = 9$ ) mice from 3 independent experiments.  $p$ -values by Mann-Whitney test; mean  $\pm$  SEM is shown.

**D** Gene expression of KLF1 measured on sorted LT-HSCs from wt ( $n = 9$ ) mice, blue; *th3/+* ( $n = 7$ ) mice, red; *th3/+* Rapa ( $n = 9$ ) mice, orange; wt Rapa ( $n = 5$ ) mice, from 3 independent experiments.  $p$ -values by Mann-Whitney test; mean  $\pm$  SEM is shown.

**E** Gene expression of KLF1 measured on sorted  $MPP^{MK/E}$  from wt ( $n = 5$ ) mice, blue; *th3/+* ( $n = 10$ ) mice, red; *th3/+* Rapa ( $n = 10$ ) mice, orange; wt Rapa ( $n = 4$ ) mice from 3 independent experiments. Relative expression on HPRT.

$P$ -values by Mann-Whitney test; mean  $\pm$  SEM is shown. **F** Percentage of Cyto-ID+ in LT-HSCs in untreated *th3/+* ( $n = 9$ ) and *th3/+* Rapa LT-HSCs ( $n = 7$ ).  $P$ -values by two-tailed unpaired  $t$ -test; mean  $\pm$  SEM is shown. **G** Quantification of CYTO-ID dye levels (MFI) in untreated *th3/+* ( $n = 9$ ) and *th3/+* Rapa LT-HSCs ( $n = 7$ ).  $p$ -value by Mann-Whitney test; mean  $\pm$  SEM is shown. **H** pS6 levels measured by flow cytometry in untreated ( $n = 6$ ) and treated *th3/+* LT-HSCs ( $n = 7$ ).  $p < 0.0001$  by two-tailed unpaired  $t$ -test; mean  $\pm$  SEM is shown. **I** Cloning efficiency of the HSC/MPP Subset1 of HD Ctrl and treated with Rapamycin (5 ng/ml). Number of colonies/2000 cells/plate from HD HSC/MPP Subset1 plated in a CFU assay with or without rapamycin ( $n = 3$  independent experiments; each dot represents the mean of 2 technical replicates). mean  $\pm$  SEM is shown. **J** Percentage of colonies generated by HSC/MPP Subset1 Ctrl and in response to treatment with Rapamycin ( $n = 3$  independent experiments). The type of colony: erythroid (E), granulocyte and myeloid (GM) or a combination of both (mix) is shown.  $P$ -value two-way ANOVA, Šidák's multiple comparisons test, mean  $\pm$  SEM is shown. Source data are provided as Source Data file.

119, Milteny Biotech). All staining (panel D or E) was performed with commercially prepared antibodies in MACS Buffer supplemented with BSA and EDTA (Milteny Biotech).

For cell-sorting experiments, cells were sorted using the MoFlow XDPs and BD FACS Aria Fusion sorters available at the San Raffaele

Flow Cytometry Core Facility, FRACTAL – Flow cytometry Resource, Advanced Cytometry Technical Applications Laboratory. Purity mode was selected and purity for all sorts was  $> 95\%$ . Unstained cells and compensation beads (BD Biosciences) were used for compensation and as a control to set appropriate gates.

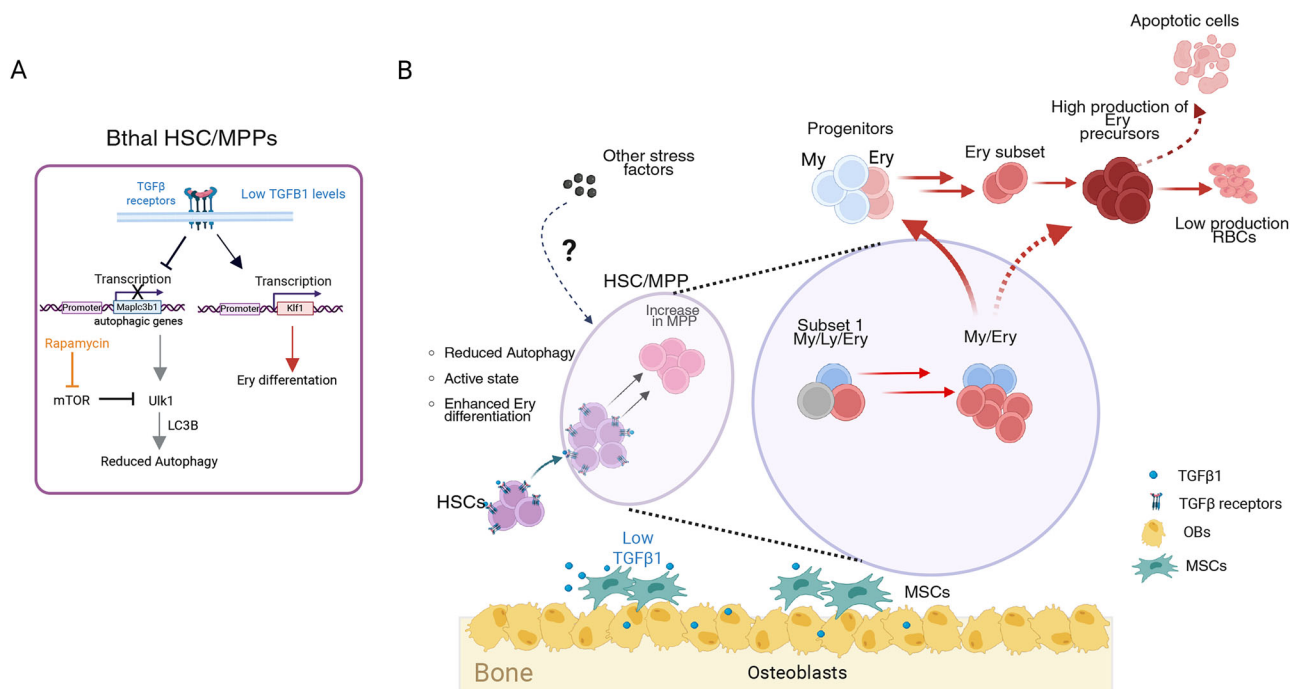


**Fig. 8 | Model of hematopoiesis in  $\beta$ -thalassemia.** In  $\beta$ -thalassemia, rare multi-potent (Ery/My/Ly) primitive cells are leaving their quiescent state and shifting towards an active status with a preferential erythroid lineage differentiation. **A**) Specifically, inhibition of TGF $\beta$  signaling leads LT-HSC towards erythroid lineage by increasing *Klf1* expression and by reducing the autophagy, in terms of *Map1lc3b* gene expression and mTOR activation. Rapamycin treatment restores the hematopoietic process by inducing autophagic activity in LT-HSCs. **B**). Low TGF $\beta$ 1 production in Bthal BM niche by MSCs and OBs causes a reduction of autophagy in

HSC, favoring the loss of stemness and an acceleration towards the erythroid lineage. A subset of cells with Ery potential can quickly differentiate in response to niche signals, thus depleting Ery cells from the progenitor fraction, or can be directly committed towards erythroid precursors. Other stress signals could contribute to the altered HSC cell fate in Bthal. TGF $\beta$ 1-dependent autophagy in Bthal HSC/MPP cells. Based on the inhibitory strategy, TGF $\beta$  signaling regulates autophagy and erythroid commitment of primitive cells. The image was created with BioRender.com. (<https://BioRender.com/99gtle>).

For in vitro treatment with TGF $\beta$ 1, Lin cells were cultured in StemSpan SFEM media (STEMCELL Technologies) for 20 h and then treated with Recombinant Mouse TGF-beta 1 Protein 10 ng/ml for 8 h<sup>88</sup> (Cat. No. 7666-MB R&D Systems) or Bafilomycin A1 5 nM for 6 h (Cat. No. B1793, Sigma). After treatment, Lin cells were stained with murine antibody panel D.

For autophagy analyses, stained cells were incubated for 15 min at 37 °C with Cyto-ID (1:1,000, Enzo, ENZ-51031-0050) in staining media. Cells were then washed with staining media and re-suspended in staining media analyzed for dye fluorescence in the FITC.

For phospho-S6 analysis, stained cells were washed in PBS, fixed in Cytotfix/Cytoperm buffer (BD Biosciences, Cat. No. 554714) for 20 min at 4 °C, washed in PermWash, and incubated in PermWash overnight at 4 °C with the following primary antibody: rabbit anti-phospho-S6 A488 (Cell Signaling, Cat. No. 4854).

Data were collected using FACSaria or FACS Canto using DIVA software (Becton Dickinson). Cell analyses were performed using FCS express 7, De Novo Software, Inc. (Becton Dickinson).

**Human antibody panels.** Panel (A): CD34/PE-Cy7 (Cat. No. #348811), CD38/PerCp-Cy5 (Cat. No. #551400), CD90/APC (Cat. No. #559869), CD45RA/FITC (Cat. No. #555488), CD135/BV421 (Cat. No. #564708), CD10/BV510 (Cat. No. #563032), CD7/APC-H7 (Cat. No. #564020); CD49f/PE-Cat. No. #555736 Panel (B): CD34/PE-Cy7 (Cat. No. #348811), CD38/PerCp-Cy5 (Cat. No. #551400), CD45RA/FITC (Cat. No. #555488), CD90/APC (Cat. No. #559869), CD10/BV510 (Cat. No. #563032), CD135/BV421 (Cat. No. #564708), BAH1/PE (Cat. No. #565746), CD71/Alexa700 (Cat. No. #563769); Panel (C): CD34/PB\* (Cat. No. #343512), CD38/PE-Cy7 (Cat. No. #560677), CD90/APC (Cat. No. #559869), CD45RA/FITC (Cat. No. #555488), CD49f/PE-Cy5 (Cat. No. #551129), CD19/Alexa700\* (Cat. No. #302226), CLEC9A/PE\* (Cat.

No. #353804); Panel (D): CD14/PE-Cy7\* (Cat. No. #301814), CD15/BV421\* (Cat. No. #125614), GlyA/PE\*\* (Cat. No. #R7078).

All antibodies were from BD except those indicated by \* and \*\*, which are from BioLegend and DAKO, respectively. All antibodies were titrated and validated using appropriate positive and negative control samples. Human subpopulations were defined as reported in Supplementary Table 1.

**Murine antibody panels.** Panel (D). Fc Block (Cat. No. #553142), Lin/Alexa700 (Cat. No. #133313)\*, Scal/PE-Cy7 (Cat. No. #558162, D7), CD117/APC (Cat. No. #553356, 2B8), CD135/BV421 (Cat. No. #135314, A2F10)\*, CD48/Alexa488 (Cat. No. #103414, HM48-1)\*, CD150/PE (Cat. No. #562651, Q38-480).

Panel (E). Fc Block (Cat. No. #553142), Ter119 FITC (Cat. No. #115921-85)\*\*\*, CD44 APC (Cat. No. #559250, Clone IM7).

All antibodies were from BD except those indicated by \* and \*\* that are from BioLegend and eBioscience, respectively. All antibodies were titrated and validated using appropriate positive and negative control samples.

**Colony-forming unit assay.** Indicated populations were sorted into 500  $\mu$ l MACS Buffer supplemented with BSA and EDTA (Milteny Biotech) in 1.5 ml microcentrifuge tubes (4000 cells/tube). Cells were then centrifuged at 500  $\times$  g for 5 min and re-suspended in 70  $\mu$ l MACS Buffer supplemented with BSA and EDTA (Milteny Biotech) and added to 2.5 ml Methocult optimum (H4034, Stem Cell Technologies) with Flt3-L 10 ng/ml and IL-6 10 ng/ml (Miltenyi Biotec). Plating was performed according to the manufacturer's protocol in SmartDishes (Stem Cell Technologies). Plates were cultured 14–16 days at 37 °C and the number of each type of CFU (myeloid, erythroid or mixed) were determined by visual inspection through microscopic analysis 14–16 days

after plating. Colonies were harvested on days 14–16 and stained with the antibody panel C.

**Gene expression analysis.** Total RNA was isolated from sorted subpopulations by AllPrep DNA/RNA Micro Kit (QIAGEN) and reverse-transcribed by Precision Nanoscript2™ Reverse Transcription Kit (PrimerDesign, Southampton, UK). Runs were performed on QX200™ Droplet Digital™ PCR (ddPCR™) System (Bio-Rad Laboratories, Inc.). Primers for Gene Expression are all from Bio-Rad Laboratories, Inc.:

*Tgfb1* mouse *Mus musculus* dMmuCPE5093564  
*Map1lc3b* mouse *Mus musculus* dMmuCPE5100062  
*Klf1* mouse *Mus musculus* dMmuCPE5103130  
*Hprt1* mouse *Mus musculus* dMmuCPE50935493  
 TGFβ1, Human, *Homo sapiens* dHsaCPE5055188  
 BMP2, Human, *Homo sapiens* dHsaCPE5053178  
 BMP4, Human, *Homo sapiens* dHsaCPE5026386  
 INHBA, Human, *Homo sapiens* dHsaCPE5049350  
 HPRT1, Human, *Homo sapiens* dHsaCPE5192872

**Immunofluorescence for LC3II.** LT-HSC were purified and sorted from CD34+ mPB samples, fixed with 4% paraformaldehyde, and stained with mouse monoclonal antibody to LC3II (NanoTools, 5F10) and DAPI. Slides were finally mounted using VectaShield (Vector Laboratories, H-1800). Images were collected on TCS SP2 Laser Scanning Confocal (Leica) and are available at the San Raffaele Advanced Light and Electron Microscopy BioImaging Center (ALEMBIC). FITC fluorescence was quantified from the images through a custom Matlab® analysis pipeline. Cells were segmented from the images of the DAPI channel through Gaussian filtering, general thresholding, and morphological operations used to close holes and smooth borders. Areas too big where further split through the watershed algorithm. For each cell mask, we measured the FITC mean and integrated intensity. Then for each cell mask, the dots in the FITC channel were segmented through a threshold so that we could also measure the area of dots for each cell and their fluorescent intensity.

**TGFβ1 ELISA.** Human TGF-β1 supernatant levels from BM platelet-poor plasma of Bthal patients and HD were determined using the Quantikine ELISA Kit (R&D Systems, DB100B) according to the manufacturer's instructions.

Murine femurs and tibias from mice were flushed with 200 μl of PBS; the flushed BM suspension was centrifuged at 500 × g for 5 min to remove BM cells. Supernatants were further clarified by spinning down at 12,000 × g for 10 min, and samples were subsequently stored at -80 °C until use. TGFβ1 BM supernatant levels were determined using the Quantikine ELISA Kit (R&D systems, MB100B) according to the manufacturer's instructions.

### Isolation of murine stromal cells and osteoblasts

Tibias and femurs previously flushed out were treated with consecutive EDTA and collagenase I (Stemcell) digestion at 37 °C to isolate stromal cells and osteoblasts. RNA was obtained using the RNeasy Mini kit (QIAGEN) and reverse transcribed as described in "Gene expression analysis" section.

**RNA sequencing.** Total RNA was isolated from human sorted subpopulations by AllPrep DNA/RNA Micro Kit (QIAGEN). 2 Pools of 2 samples for condition/subpopulations were profiled. We profiled HSCs (range 18,400–39,000), MPPs (range 16,000–50,500), Ery-CMPs (range 1000–10,000), Ery-MEPs (range 1550–8500) and GMPs (range 5000–1,800). Library was prepared using 'Ovation SoLo RNA-seq kit' (NuGEN, San Carlos, CA), following the manufacturer's instructions, starting with 1 ng of RNA as input. The SoLo RNA-Seq System uses a

unique molecular identifier (UMI) composed of 8 random bases for unambiguous identification of unique library molecules and to discriminate between true PCR duplicates and independent adaptor ligation events to fragments with the same start site.

Quality and quantity of RNA samples were determined using the Agilent 2100 Bioanalyzer RNA assay (Agilent Technologies, Santa Clara, CA) also integrating DNase treatment to minimize adverse effects on assay performance and data quality. Indeed, final libraries were checked with Qubit 2.0 Fluorometer (Invitrogen, Carlsbad, CA) and Agilent Bioanalyzer DNA assay. Libraries were processed and sequenced (125bp-pair-end) on HiSeq2500 (Illumina, San Diego, CA), with production of 85.2 M reads per sample on average. The CASAVA 1.8.2 version of the Illumina pipeline was used to process raw data for both form conversion and de-multiplexing.

Gene expression RNA-seq data have been deposited in the GEO repository with accession number [GSE263306](https://www.ncbi.nlm.nih.gov/geo/query/acc.cgi?acc=GSE263306).

RNAseq analysis on sorted murine HSCs is described in ref. 23. Gene expression RNA-seq data have been deposited in the European Nucleotide Archive database with accession numbers [PRJEB31882](https://www.ebi.ac.uk/ena/record/PRJEB31882).

### BMP-RE target gene identification

To identify DEGs that are involved in the erythroid differentiation process and could be targets of BMP regulatory elements and are involved in erythroid differentiation process, we extracted all DEGs list (padj <0.01) from differential tests performed between 4 consecutive erythroid differentiation timepoints from ref. 36. Hence, we looked for genes having BMP (GGCGCC) regulatory elements sequences 2Kbp upstream from their TSS. We identified 3468 erythroid genes carrying BMP-RE. For each DEG we matched FDR and logFC from HSC\_MPP (BThal vs HD) differential gene test (EdgeR + DESeq2). We then performed Over Representation Analysis test using Gene Ontology dataset, using as query gene set the DEGs from Bthal vs HD that contain BMP regulatory elements.

### MuSiC deconvolution

To identify the presence of an early erythroid signature in HSC/MPPs in the Thal group compared to healthy group, we evaluated the cell-type proportions in our bulk RNA-seq experiment by leveraging single-cell data provided by ref. 41 Tusi BK. et al., Nature, 2018. Bulk RNA-seq deconvolution was performed using the R package Multi-subject Single Cell deconvolution R package (MuSiC, v0.1.1)<sup>40</sup> starting from raw counts as instructed in the package. We considered 4 murine populations identified by scRNA-seq in ref. 41: CD71high P1, P1, P2, and P5, which correspond to late CFUe, CFUe (CEP), BFUe, and less-differentiated mixed myeloid colonies, respectively<sup>41</sup>. Since our bulk RNA-seq is performed on human subpopulations and single-cell data from ref. 41 is on murine subpopulations, we prepared the scRNAseq raw counts matrix by converting mouse symbols into human ones using the R package 'nichenetr'. To avoid low-expressed genes, we discard genes with total expression across all cells (scRNA-seq) lower than 10 and total expression across all samples (bulk RNA-seq) less than 25.

### Sample preparation for scRNAseq

Frozen MNCs or BM CD34+ cells were thawed in the water bath, immediately followed by drop-wise addition of 10x the volume of pre-warmed IMDM (Life Technologies) + 0.1 mg/ml DNase (Worthington) + 50% Fetal Bovine Serum (FBS, Life Technologies).

After centrifugation and cell counting, cells were resuspended in 50 μl PBS/3%FBS and blocked with 5 μl Human TruStain FcX™ Fc Blocking Reagent (BioLegend) per 1×10<sup>6</sup> cells for 10 min at 4 °C. Then, 50 μl phenotyping antibody mix (diluted in PBS/3%FBS as indicated) per 1×10<sup>6</sup> cells was directly added: Zombie aqua (BioLegend, Cat#423101, 1:1000); CD123BV785 (BioLegend, Cat#306032, 1:100); CD34 APC-Cy7 (BioLegend, Cat#343514, 1:100); CD38 PE-C7

(BioLegend, Cat#303516, 1:100); CD90APC (BD Pharmingen, Cat#559869, 1:100); CD45RA A700 (BioLegend, Cat#304120, 1:300); CD49fPE-Cy5 (BD Pharmingen, Cat#551129, 1:100); CD19 BV421 (BioLegend, Cat#302233, 1:400); CD71 FITC (BioLegend, Cat#334104, 1:1000); CD117 BV650 (BD Horizon, Cat#563466, 1:100); BAH-IPE (BD Pharmingen, Cat#565746, 1:50). Additionally, for certain donors, a different TotalSeq™ Hashtag antibody (BioLegend, Cat #394631, 394633, 394637, 394641, 394643 or 394645) was added at a concentration of 0.5 µg / 1×10<sup>6</sup> cells. Of note, Hashtag staining was unsatisfying and therefore Hashtag were not used in any of the analysis.

After incubation for 30 min at 4 °C, cells were washed three times with PBS/3%FBS, then resuspended in PBS/3%FBS and filtered for flow cytometry. Total CD34<sup>+</sup> cells (gate: size/singlets/ Zombie-negative/CD34-positive cells) or phenotypic HSC/MPPs (gate: size/singlets/ Zombie-negative/CD34-positive/bottom 10-20% CD38-low cells, CD45RA-) were sorted using the BD FACSAria Fusion (all samples from SR-TIGET), Sony sorter or the BD FACSAria III (donors P181, P185, and P257, UCL). The average sort purity was >95%.

After the sort, up to 20,000 CD34<sup>+</sup> cells were pooled with up to 10,000 phenotypic HSC/MPPs from different donors. In the case of the HD samples P181, P185, and P257 no pooling was performed, and up to 20,000 were used. After centrifugation, cells were resuspended in 47 µl PBS + 0.04% BSA for library prep using the Chromium™ Single Cell 3' reagents. Cells were immediately processed for single-cell sequencing using the Chromium™ Single Cell 3' Library & Gel Bead Kit v3 (10x Genomics) following the manufacturer's protocols. RNA and cell surface protein (hashtag) libraries were generated following the manufacturer's protocols (10x Genomics and BioLegend, respectively). Libraries from multiple samples were combined prior to sequencing and sequenced on the Illumina NovaSeq 6000 system, aiming for a minimum of 40,000 reads per cell for gene expression and 10,000 reads per cell for cell surface protein.

### scRNAseq analysis

Reads demultiplexing, aligning, and UMI quantification: the samples from our 10 donors (healthy\_CTRL, P185, P181, P257, B10059062019, 10060062019, 60041052018, 60166112019, 60133072019, 60170112019) were pooled and sequenced across 4 sequencing runs on the Illumina NovaSeq 6000 system. The resulting scRNA-seq reads were then aligned to the GRCh37 (hg19) reference (refdata-cellranger-hg19-3.0.0 - Ensembl 87) and quantified through the use of "cellranger count" from the 10x Genomics Cell Ranger 6.0.1 pipeline<sup>89</sup>. Two more pediatric bone marrow healthy control samples<sup>42</sup>, were also added to the analysis. Their previously aligned and quantified libraries were downloaded from <https://www.ncbi.nlm.nih.gov/geo/query/acc.cgi?acc=GSE155259>, respectively the samples GSM44698254 and GSM44698255.

### Statistical analysis

Statistical analyses were performed by using GraphPad prism v10.0 software (La Jolla, CA, USA). All data are presented as mean ± SEM, as stated in the figure legends. One or Two-tailed unpaired Student's t-tests or Mann-Whitney test were used to compare two groups, and all other specific statistical tests are indicated in figure legends. Figure legends and the Source data file contain information on statistical tests, sample sizes, and P-values. No statistical method was used to predetermine the sample size.

### Reporting summary

Further information on research design is available in the Nature Portfolio Reporting Summary linked to this article.

### Data availability

Gene expression human RNA-seq has been deposited in the GEO repository with accession number [GSE263306](https://www.ncbi.nlm.nih.gov/geo/query/acc.cgi?acc=GSE263306). RNAseq analysis on

sorted murine HSCs is described in ref. 23. Gene expression RNA-seq data have been deposited in Ethe uropean Nucleotide Archive database with accession numbers [PRJEB31882](https://www.ncbi.nlm.nih.gov/geo/query/acc.cgi?acc=PRJEB31882). Gene expression human scRNA-seq data have been deposited in the GEO repositories with accession numbers [GSE247738](https://www.ncbi.nlm.nih.gov/geo/query/acc.cgi?acc=GSE247738) for the samples P185, P257, and P185 (GSM7900108, GSM7900109, and GSM7900110, respectively) and [GSE263204](https://www.ncbi.nlm.nih.gov/geo/query/acc.cgi?acc=GSE263204) for the samples HD, B10059062019, B10060062019, B60041052018, B60166112019, B60133072019, B60170112019). Data and materials availability: the authors declare that all relevant data supporting the findings of this study are available within the paper, in its supplementary information file, and Source Data File. Source data are provided with this paper.

### Code availability

The code related to the generated data is available in the following GitLab repository. [http://www.bioinfotiget.it/gitlab/custom/lidonnici\\_naturecomm2025](http://www.bioinfotiget.it/gitlab/custom/lidonnici_naturecomm2025).

### References

1. Velten, L. et al. Human haematopoietic stem cell lineage commitment is a continuous process. *Nat. Cell Biol.* **19**, 271–281 (2017).
2. Akashi, K., Traver, D., Miyamoto, T. & Weissman, I. L. A clonogenic common myeloid progenitor that gives rise to all myeloid lineages. *Nature* **404**, 193–197 (2000).
3. Doulatov, S., Notta, F., Laurenti, E. & Dick, J. E. Hematopoiesis: a human perspective. *Cell Stem Cell* **10**, 120–136 (2012).
4. Busch, K. et al. Fundamental properties of unperturbed haematopoiesis from stem cells in vivo. *Nature* **518**, 542–546 (2015).
5. Haas, S., Trumpp, A. & Milsom, M. D. Causes and consequences of hematopoietic stem cell heterogeneity. *Cell Stem Cell* **22**, 627–638 (2018).
6. Laurenti, E. & Gottgens, B. From haematopoietic stem cells to complex differentiation landscapes. *Nature* **553**, 418–426 (2018).
7. Sanjuan-Pla, A. et al. Platelet-biased stem cells reside at the apex of the haematopoietic stem-cell hierarchy. *Nature* **502**, 232–236 (2013).
8. Carrelha, J. et al. Hierarchically related lineage-restricted fates of multipotent haematopoietic stem cells. *Nature* **554**, 106–111 (2018).
9. Perie, L., Duffy, K. R., Kok, L., de Boer, R. J. & Schumacher, T. N. The branching point in erythro-myeloid differentiation. *Cell* **163**, 1655–1662 (2015).
10. Notta, F. et al. Distinct routes of lineage development reshape the human blood hierarchy across ontogeny. *Science* **351**, aab2116 (2016).
11. Belluschi, S. et al. Myelo-lymphoid lineage restriction occurs in the human haematopoietic stem cell compartment before lymphoid-primed multipotent progenitors. *Nat. Commun.* **9**, 4100 (2018).
12. Haas, S. et al. Inflammation-induced emergency megakaryopoiesis driven by hematopoietic stem cell-like megakaryocyte progenitors. *Cell Stem Cell* **17**, 422–434 (2015).
13. Wilson, A. et al. Hematopoietic stem cells reversibly switch from dormancy to self-renewal during homeostasis and repair. *Cell* **135**, 1118–1129 (2008).
14. Simsek, T. et al. The distinct metabolic profile of hematopoietic stem cells reflects their location in a hypoxic niche. *Cell Stem Cell* **7**, 380–390 (2010).
15. Ho, T. T. et al. Autophagy maintains the metabolism and function of young and old stem cells. *Nature* **543**, 205–210 (2017).
16. Vasto, S. et al. Inflammatory networks in ageing, age-related diseases and longevity. *Mech. Ageing Dev.* **128**, 83–91 (2007).
17. King, K. Y. & Goodell, M. A. Inflammatory modulation of HSCs: viewing the HSC as a foundation for the immune response. *Nat. Rev. Immunol.* **11**, 685–692 (2011).

18. Bogeska, R. et al. Inflammatory exposure drives long-lived impairment of hematopoietic stem cell self-renewal activity and accelerated aging. *Cell Stem Cell* **29**, 1273–1284.e1278 (2022).
19. Fanti, A. K. et al. Flt3- and Tie2-Cre tracing identifies regeneration in sepsis from multipotent progenitors but not hematopoietic stem cells. *Cell Stem Cell* **30**, 207–218.e207 (2023).
20. Munz, C. M. et al. Regeneration after blood loss and acute inflammation proceeds without contribution of primitive HSCs. *Blood* **141**, 2483–2492 (2023).
21. Taher, A. T., Musallam, K. M. & Cappellini, M. D. beta-Thalassemias. *N. Engl. J. Med* **384**, 727–743 (2021).
22. Crippa, S. et al. Bone marrow stromal cells from beta-thalassemia patients have impaired hematopoietic supportive capacity. *J. Clin. Invest* **129**, 1566–1580 (2019).
23. Aprile, A. et al. Hematopoietic stem cell function in beta-thalassemia is impaired and is rescued by targeting the bone marrow niche. *Blood* **136**, 610–622 (2020).
24. Mende, N. et al. Unique molecular and functional features of extramedullary hematopoietic stem and progenitor cell reservoirs in humans. *Blood* **139**, 3387–3401 (2022).
25. Laurenti, E. et al. The transcriptional architecture of early human hematopoiesis identifies multilevel control of lymphoid commitment. *Nat. Immunol.* **14**, 756–763 (2013).
26. Qian, P. et al. The Dlk1-Gtl2 Locus preserves LT-HSC function by inhibiting the PI3K-mTOR pathway to restrict mitochondrial metabolism. *Cell Stem Cell* **18**, 214–228 (2016).
27. Blank, U. & Karlsson, S. TGF-beta signaling in the control of hematopoietic stem cells. *Blood* **125**, 3542–3550 (2015).
28. Sun, D. et al. Epigenomic profiling of young and aged HSCs reveals concerted changes during aging that reinforce self-renewal. *Cell Stem Cell* **14**, 673–688 (2014).
29. Mirantes, C., Passegue, E. & Pietras, E. M. Pro-inflammatory cytokines: emerging players regulating HSC function in normal and diseased hematopoiesis. *Exp. Cell Res* **329**, 248–254 (2014).
30. Smith-Berdan, S. et al. Robo4 cooperates with CXCR4 to specify hematopoietic stem cell localization to bone marrow niches. *Cell Stem Cell* **8**, 72–83 (2011).
31. Sugimura, R. et al. Noncanonical Wnt signaling maintains hematopoietic stem cells in the niche. *Cell* **150**, 351–365 (2012).
32. Wilson, A. et al. c-Myc controls the balance between hematopoietic stem cell self-renewal and differentiation. *Genes Dev.* **18**, 2747–2763 (2004).
33. Westendorp, B. et al. E2F7 represses a network of oscillating cell cycle genes to control S-phase progression. *Nucleic Acids Res.* **40**, 3511–3523 (2012).
34. Clijsters, L. et al. Cyclin F controls cell-cycle transcriptional outputs by directing the degradation of the three activator E2Fs. *Mol. Cell* **74**, 1264–1277.e1267 (2019).
35. Pietras, E. M., Warr, M. R. & Passegue, E. Cell cycle regulation in hematopoietic stem cells. *J. Cell Biol.* **195**, 709–720 (2011).
36. Schulz, V. P. et al. A unique epigenomic landscape defines human erythropoiesis. *Cell Rep.* **28**, 2996–3009.e2997 (2019).
37. Chen, L. et al. Transcriptional diversity during lineage commitment of human blood progenitors. *Science* **345**, 1251033 (2014).
38. Moroy, T., Vassen, L., Wilkes, B. & Khandanpour, C. From cytopenia to leukemia: the role of Gfi1 and Gfi1b in blood formation. *Blood* **126**, 2561–2569 (2015).
39. Palii, C. G. et al. Single-cell proteomics reveal that quantitative changes in co-expressed lineage-specific transcription factors determine cell fate. *Cell Stem Cell* **24**, 812–820.e815 (2019).
40. Wang, X., Park, J., Susztak, K., Zhang, N. R. & Li, M. Bulk tissue cell type deconvolution with multi-subject single-cell expression reference. *Nat. Commun.* **10**, 380 (2019).
41. Tusi, B. K. et al. Population snapshots predict early haematopoietic and erythroid hierarchies. *Nature* **555**, 54–60 (2018).
42. Roy, A. et al. Transitions in lineage specification and gene regulatory networks in hematopoietic stem/progenitor cells over human development. *Cell Rep.* **36**, 109698 (2021).
43. Zeng, A. G. X. et al. Precise single-cell transcriptomic mapping of normal and leukemic cell states reveals unconventional lineage priming in acute myeloid leukemia. *bioRxiv* (2023). <https://doi.org/10.1101/2023.12.26.573390>.
44. Zhang, Y. W. et al. Hyaluronic acid-GPRC5C signalling promotes dormancy in haematopoietic stem cells. *Nat. Cell Biol.* **24**, 1038–1048 (2022).
45. Lange, M. et al. CellRank for directed single-cell fate mapping. *Nat. Methods* **19**, 159–170 (2022).
46. Van den Berge, K. et al. Trajectory-based differential expression analysis for single-cell sequencing data. *Nat. Commun.* **11**, 1201 (2020).
47. Zermati, Y. et al. Transforming growth factor inhibits erythropoiesis by blocking proliferation and accelerating differentiation of erythroid progenitors. *Exp. Hematol.* **28**, 885–894 (2000).
48. Naka, K. & Hirao, A. Regulation of Hematopoiesis and Hematological Disease by TGF-beta Family Signaling Molecules. *Cold Spring Harb. Perspect. Biol.* **9**, a027987 (2017).
49. Soderberg, S. S., Karlsson, G. & Karlsson, S. Complex and context dependent regulation of hematopoiesis by TGF-beta superfamily signaling. *Ann. N. Y. Acad. Sci.* **1176**, 55–69 (2009).
50. Tecalco-Cruz, A. C., Rios-Lopez, D. G., Vazquez-Victorio, G., Rosales-Alvarez, R. E. & Macias-Silva, M. Transcriptional cofactors Ski and SnoN are major regulators of the TGF-beta/Smad signaling pathway in health and disease. *Signal Transduct. Target Ther.* **3**, 15 (2018).
51. Zhang, S. et al. Smad7 antagonizes transforming growth factor beta signaling in the nucleus by interfering with functional Smad-DNA complex formation. *Mol. Cell Biol.* **27**, 4488–4499 (2007).
52. Blank, U. & Karlsson, S. The role of Smad signaling in hematopoiesis and translational hematology. *Leukemia* **25**, 1379–1388 (2011).
53. Fortunel, N. O., Hatzfeld, A. & Hatzfeld, J. A. Transforming growth factor-beta: pleiotropic role in the regulation of hematopoiesis. *Blood* **96**, 2022–2036 (2000).
54. Klamer, S. E. et al. TGFBI expressed by bone marrow niche cells and hematopoietic stem and progenitor cells regulates hematopoiesis. *Stem Cells Dev.* **27**, 1494–1506 (2018).
55. Maguer-Satta, V. et al. Regulation of human erythropoiesis by activin A, BMP2, and BMP4, members of the TGFbeta family. *Exp. Cell Res* **282**, 110–120 (2003).
56. Laperrousaz, B. et al. Primitive CML cell expansion relies on abnormal levels of BMPs provided by the niche and on BMPRIb overexpression. *Blood* **122**, 3767–3777 (2013).
57. Zhou, L. et al. Inhibition of the TGF-beta receptor I kinase promotes hematopoiesis in MDS. *Blood* **112**, 3434–3443 (2008).
58. Dussiot, M. et al. An activin receptor IIA ligand trap corrects ineffective erythropoiesis in beta-thalassemia. *Nat. Med* **20**, 398–407 (2014).
59. Ning, J., Zhao, Y., Ye, Y. & Yu, J. Opposing roles and potential antagonistic mechanism between TGF-beta and BMP pathways: Implications for cancer progression. *EBioMedicine* **41**, 702–710 (2019).
60. Guo, X. & Wang, X. F. Signaling cross-talk between TGF-beta/BMP and other pathways. *Cell Res* **19**, 71–88 (2009).
61. Yang, J., Carra, S., Zhu, W. G. & Kampinga, H. H. The regulation of the autophagic network and its implications for human disease. *Int J. Biol. Sci.* **9**, 1121–1133 (2013).
62. Yang, B. et al. A mouse model for beta O-thalassemia. *Proc. Natl Acad. Sci. USA* **92**, 11608–11612 (1995).

63. Aprile, A. et al. Inhibition of FGF23 is a therapeutic strategy to target hematopoietic stem cell niche defects in beta-thalassemia. *Sci. Transl. Med.* **15**, eabq3679 (2023).
64. Kiyono, K. et al. Autophagy is activated by TGF-beta and potentiates TGF-beta-mediated growth inhibition in human hepatocellular carcinoma cells. *Cancer Res.* **69**, 8844–8852 (2009).
65. Chang, K. et al. TGF-beta/INHB/actin signaling regulates age-dependent autophagy and cardiac health through inhibition of mTORC2. *Autophagy* **16**, 1807–1822 (2020).
66. Trelford, C. B. & Di Guglielmo, G. M. Canonical and Non-canonical TGFbeta Signaling Activate Autophagy in an ULK1-Dependent Manner. *Front. Cell Dev. Biol.* **9**, 712124 (2021).
67. Lechauve, C. et al. The autophagy-activating kinase ULK1 mediates clearance of free alpha-globin in beta-thalassemia. *Sci. Transl. Med.* **11**, eaav4881 (2019).
68. Pietras, E. M. et al. Functionally distinct subsets of lineage-biased multipotent progenitors control blood production in normal and regenerative conditions. *Cell Stem Cell* **17**, 35–46 (2015).
69. Laurenti, E. et al. CDK6 levels regulate quiescence exit in human hematopoietic stem cells. *Cell Stem Cell* **16**, 302–313 (2015).
70. Cheng, T. et al. Hematopoietic stem cell quiescence maintained by p21cip1/waf1. *Science* **287**, 1804–1808 (2000).
71. Di Tullio, A., Passaro, D., Rouault-Pierre, K., Purewal, S. & Bonnet, D. Nuclear factor Erythroid 2 regulates human HSC self-renewal and t cell differentiation by preventing NOTCH1 activation. *Stem Cell Rep.* **9**, 5–11 (2017).
72. Bataller, A., Montalban-Bravo, G., Soltysiak, K. A. & Garcia-Manero, G. The role of TGFbeta in hematopoiesis and myeloid disorders. *Leukemia* **33**, 1076–1089 (2019).
73. Hinge, A. & Filippi, M. D. Deconstructing the complexity of TGFbeta signaling in hematopoietic stem cells: quiescence and beyond. *Curr. Stem Cell Rep.* **2**, 388–397 (2016).
74. Seoane, J. et al. TGFbeta influences Myc, Miz-1 and Smad to control the CDK inhibitor p15INK4b. *Nat. Cell Biol.* **3**, 400–408 (2001).
75. Staller, P. et al. Repression of p15INK4b expression by Myc through association with Miz-1. *Nat. Cell Biol.* **3**, 392–399 (2001).
76. Challen, G. A., Boles, N. C., Chambers, S. M. & Goodell, M. A. Distinct hematopoietic stem cell subtypes are differentially regulated by TGF-beta1. *Cell Stem Cell* **6**, 265–278 (2010).
77. Perry, J. M., Harandi, O. F. & Paulson, R. F. BMP4, SCF, and hypoxia cooperatively regulate the expansion of murine stress erythroid progenitors. *Blood* **109**, 4494–4502 (2007).
78. Crane, J. L. & Cao, X. Bone marrow mesenchymal stem cells and TGF-beta signaling in bone remodeling. *J. Clin. Invest.* **124**, 466–472 (2014).
79. Valletta, S. et al. Micro-environmental sensing by bone marrow stroma identifies IL-6 and TGFbeta1 as regulators of hematopoietic ageing. *Nat. Commun.* **11**, 4075 (2020).
80. Kuhikar, R. et al. Transforming growth factor beta1 accelerates and enhances in vitro red blood cell formation from hematopoietic stem cells by stimulating mitophagy. *Stem Cell Res. Ther.* **11**, 71 (2020).
81. Stolla, M. C. et al. ATG4A regulates human erythroid maturation and mitochondrial clearance. *Blood Adv.* **6**, 3579–3589 (2022).
82. Sandoval, H. et al. Essential role for Nix in autophagic maturation of erythroid cells. *Nature* **454**, 232–235 (2008).
83. Etzrodt, M. et al. Inflammatory signals directly instruct PU.1 in HSCs via TNF. *Blood* **133**, 816–819 (2019).
84. Yamashita, M. & Passegue, E. TNF-alpha coordinates hematopoietic stem cell survival and myeloid regeneration. *Cell Stem Cell* **25**, 357–372.e357 (2019).
85. Baldrige, M. T., King, K. Y., Boles, N. C., Weksberg, D. C. & Goodell, M. A. Quiescent haematopoietic stem cells are activated by IFN-gamma in response to chronic infection. *Nature* **465**, 793–797 (2010).
86. Suragani, R. N. et al. Transforming growth factor-beta superfamily ligand trap ACE-536 corrects anemia by promoting late-stage erythropoiesis. *Nat. Med.* **20**, 408–414 (2014).
87. Courbon, G. et al. Bone-derived C-terminal FGF23 cleaved peptides increase iron availability in acute inflammation. *Blood* **142**, 106–118 (2023).
88. Santaguida, M. et al. JunB protects against myeloid malignancies by limiting hematopoietic stem cell proliferation and differentiation without affecting self-renewal. *Cancer Cell* **15**, 341–352 (2009).
89. Zheng, G. X. et al. Massively parallel digital transcriptional profiling of single cells. *Nat. Commun.* **8**, 14049 (2017).

## Acknowledgements

We thank Cesare Covino and Cammarota Eugenia for imaging at the ALEMBIC facility, an advanced microscopy laboratory established by IRCCS Ospedale San Raffaele and Università Vita-Salute San Raffaele. We thank the Fractal facility for their flow cytometry services at IRCCS Ospedale San Raffaele. We also thank the BRC E6 hub at the University of Cambridge for their flow cytometry services, and the team at the Cancer Research UK Cambridge Institute Genomics Core Facility for 10x Genomics libraries and high-throughput sequencing. We thank Mariana Quiroga Londono for help with transferring raw scRNAseq files and Rebecca Hannah for help with depositing scRNA-seq data to GEO. Finally, we thank Laura Silvestri for discussing data on the TGFβ/BMP pathway. This work was supported by Telethon SR-TIGET Core Grant 2022-2026 to G.F. and MRL. E.L. is funded by a Sir Henry Dale Fellowship jointly funded by the Wellcome Trust and the Royal Society (107630/Z/15/A). N.M. was supported by the Japan Society for the Promotion of Science (JSPS) Short-term Postdoctoral Fellowship and by a DFG Research Fellowship (ME 5209/1-1). B.G. group was funded by Wellcome (206328/Z/17/Z) and the MRC (MR/M008975/1 and MR/S036113/1). This research was funded in whole, or in part, by the Wellcome Trust (203151/Z/16/Z, 203151/A/16/Z, 215116/Z/18/Z) and the UKRI Medical Research Council (MC\_PC\_17230). For the purpose of open access, the author has applied a CC BY public copyright licence to any Author Accepted Manuscript version arising from this submission.

## Author contributions

M.R.L. designed the experimental work, coordinated the project, performed research, analyzed data and wrote the paper; G.C. contributed to design and perform research, discussed data and wrote the paper; N.M. contributed to the scRNAseq samples processing and analysis, to cell sorting, scRNAseq processing and analysis of 3 pediatric HD samples; H.B. performed all of the scRNAseq analysis; M.B. and I.M. performed bioinformatic analysis on the RNAseq data; M.S. and V.R. performed in vivo experiments; F.T. contributed to experimental work; N.K.W. processed 2 pediatric HD samples for scRNAseq; S.C. performed isolation of MSCs; S.S. and C.R. isolated CD34+ cells from human samples; R.L. performed experiments on murine niche components; A.A. performed RNAseq on murine cells; C.L. and J. K. performed experiments with Ulk1-/- mice; B.G. supervised N.K.W. and coordinated all the work on 3 pediatric samples; D.I., provided access and processed to 3 pediatric samples; I.R. and T.K. provided access to 3 pediatric samples; M.J.W. discussed the data and contributed to writing and critically reviewing the paper; M.E.B supervised S.C.; F.C., A.A.I. and S.M. had clinical responsibility of the patients and provided human samples; E.L. supervised N.M., H.B., coordinated all of the scRNAseq, analyzed data, edited the manuscript, and critically reviewed the paper; G.F. provided project coordination and financial support, analyzed data, wrote, and critically reviewed the paper. All authors approved the final version of the manuscript.

## Competing interests

The authors declare no competing interests.

## Additional information

**Supplementary information** The online version contains supplementary material available at <https://doi.org/10.1038/s41467-025-60676-7>.

**Correspondence** and requests for materials should be addressed to Maria Rosa Lidonnici or Giuliana Ferrari.

**Peer review information** *Nature Communications* thanks Vignir Helgason and the other anonymous reviewer(s) for their contribution to the peer review of this work. A peer review file is available.

**Reprints and permissions information** is available at <http://www.nature.com/reprints>

**Publisher's note** Springer Nature remains neutral with regard to jurisdictional claims in published maps and institutional affiliations.

**Open Access** This article is licensed under a Creative Commons Attribution-NonCommercial-NoDerivatives 4.0 International License, which permits any non-commercial use, sharing, distribution and reproduction in any medium or format, as long as you give appropriate credit to the original author(s) and the source, provide a link to the Creative Commons licence, and indicate if you modified the licensed material. You do not have permission under this licence to share adapted material derived from this article or parts of it. The images or other third party material in this article are included in the article's Creative Commons licence, unless indicated otherwise in a credit line to the material. If material is not included in the article's Creative Commons licence and your intended use is not permitted by statutory regulation or exceeds the permitted use, you will need to obtain permission directly from the copyright holder. To view a copy of this licence, visit <http://creativecommons.org/licenses/by-nc-nd/4.0/>.

© The Author(s) 2025